nature neuroscience

ARTICLES

https://doi.org/10.1038/s41593-017-0057-1

Corrected: Publisher Correction

N^6-methyladenosine RNA modification regulates embryonic neural stem cell self-renewal through histone modifications

Yang Wang[1], Yue Li[2], Minghui Yue[3,4], Jun Wang[1], Sandeep Kumar[5], Robert J. Wechsler-Reya[1], Zhaolei Zhang[6], Yuya Ogawa[3,4], Manolis Kellis[2], Gregg Duester[5] and Jing Crystal Zhao[1*]

Internal N^6-methyladenosine (m^6A) modification is widespread in messenger RNAs (mRNAs) and is catalyzed by heterodimers of methyltransferase-like protein 3 (Mettl3) and Mettl14. To understand the role of m^6A in development, we deleted *Mettl14* in embryonic neural stem cells (NSCs) in a mouse model. Phenotypically, NSCs lacking *Mettl14* displayed markedly decreased proliferation and premature differentiation, suggesting that m^6A modification enhances NSC self-renewal. Decreases in the NSC pool led to a decreased number of late-born neurons during cortical neurogenesis. Mechanistically, we discovered a genome-wide increase in specific histone modifications in *Mettl14* knockout versus control NSCs. These changes correlated with altered gene expression and observed cellular phenotypes, suggesting functional significance of altered histone modifications in knockout cells. Finally, we found that m^6A regulates histone modification in part by destabilizing transcripts that encode histone-modifying enzymes. Our results suggest an essential role for m^6A in development and reveal m^6A-regulated histone modifications as a previously unknown mechanism of gene regulation in mammalian cells.

Post-transcriptional modification of mRNA has emerged as an important mechanism for gene regulation. Among internal mRNA modifications, m^6A is by far the most abundant, tagging over 10,000 mRNAs and long noncoding RNAs[1,2]. It is a reversible modification, and both methyltranferases and demethylases have been reported. In 2014, we and others reported that Mettl3 and Mettl14 formed a heterodimer and served as core components of m^6A methyltransferase[3,4]. Both Mettl3 and Mettl14 are required for m^6A formation: in the heterodimer, Mettl3 is the enzymatic subunit and Mettl14 is required for RNA substrate recognition and maintenance of proper Mettl3 conformation[5–7].

The functional role of m^6A in gene expression regulation has been studied extensively[8], but its importance in development at organismal levels remains largely unknown. Recently, two studies reported that children born with homozygous missense mutations in the gene *FTO* (fat mass and obesity-associated protein), which encodes an m^6A demethylase[9], display severe neurodevelopmental disorders, including microcephaly, functional brain deficits and psychomotor delay, suggesting an essential, yet unexplored, role of m^6A RNA modification in brain development[10,11]. To investigate potential m^6A function in early neuronal development, we deleted *Mettl14* in mouse embryonic NSCs, as self-renewing and multipotent NSCs give rise to the entire brain, and defects in NSC activities have been shown to underlie various neurodevelopmental disorders[12]. In vitro, NSCs lacking *Mettl14* displayed robust decreases in proliferation accompanied by premature differentiation, suggesting that m^6A is required for NSC self-renewal. Consistent with this, in vivo analysis in *Mettl14*-null embryos revealed that NSCs, which are also known as radial glial cells (RGCs), in the ventricular zone (VZ) showed a decrease in number relative to those seen in control mice, and this reduction was accompanied by fewer late-born cortical neurons. Mechanistically, we observed a genome-wide increase in specific histone modifications in *Mettl14*-knockout (KO) NSCs. Notably, gene-by-gene analysis suggested that those changes were correlated with changes in gene expression and observed developmental phenotypes, suggesting that m^6A-regulated histone modification underlies alterations in NSC gene expression and activity. Finally, we present evidence that m^6A regulation of histone modification alters the stability of mRNAs encoding histone modifiers. Overall, our results show, for the first time, a key role for mRNA modification in NSCs and brain development.

Results

***Mettl14* knockout decreases NSC proliferation and promotes premature NSC differentiation in vitro.** To assess *Mettl14* loss of function in vivo, we generated *Mettl14*–conditional knockout mice (*Mettl14*$^{f/f}$) by flanking *Mettl14* exon 2 with *loxP* sites. Cre-mediated exon 2 excision results in an out-of-frame mutation that abolishes Mettl14 function (Supplementary Fig. 1a,b). To assess whether the KO strategy deletes *Mettl14* in vivo, we evaluated whether *Mettl14* was deleted globally using *EIIa-cre* transgenic mice, which express Cre at zygotic stages (Supplementary Fig. 1c,d). *Mettl14*$^{+/-}$ heterozygotes were viable and fertile and exhibited no discernible morphological or growth abnormalities, whereas no *Mettl14*$^{-/-}$ offspring were observed after crosses of *Mettl14*$^{+/-}$ mice (Supplementary Table 1). We then collected embryos resulting from crosses of heterozygotes at embryonic day 7.5 (E7.5), E8.5 and E9.5 for genotyping. *Mettl14*$^{-/-}$ embryos were identified at Mendelian ratios when we

[1]Tumor Initiation and Maintenance Program, NCI-designated Cancer Center, Sanford Burnham Prebys Medical Discovery Institute, La Jolla, CA, USA. [2]Computer Science and Artificial Intelligence Laboratory, Massachusetts Institute of Technology, Cambridge, MA, USA. [3]Division of Reproductive Sciences, Division of Developmental Biology, Perinatal Institute, Cincinnati Children's Hospital Medical Center, Cincinnati, OH, USA. [4]Department of Pediatrics, University of Cincinnati, Cincinnati, OH, USA. [5]Development, Aging, and Regeneration Program, Sanford Burnham Prebys Medical Discovery Institute, La Jolla, CA, USA. [6]Department of Molecular Genetics, The Donnelly Centre, University of Toronto, Toronto, Ontario, Canada. *e-mail: czhao@sbpdiscovery.org

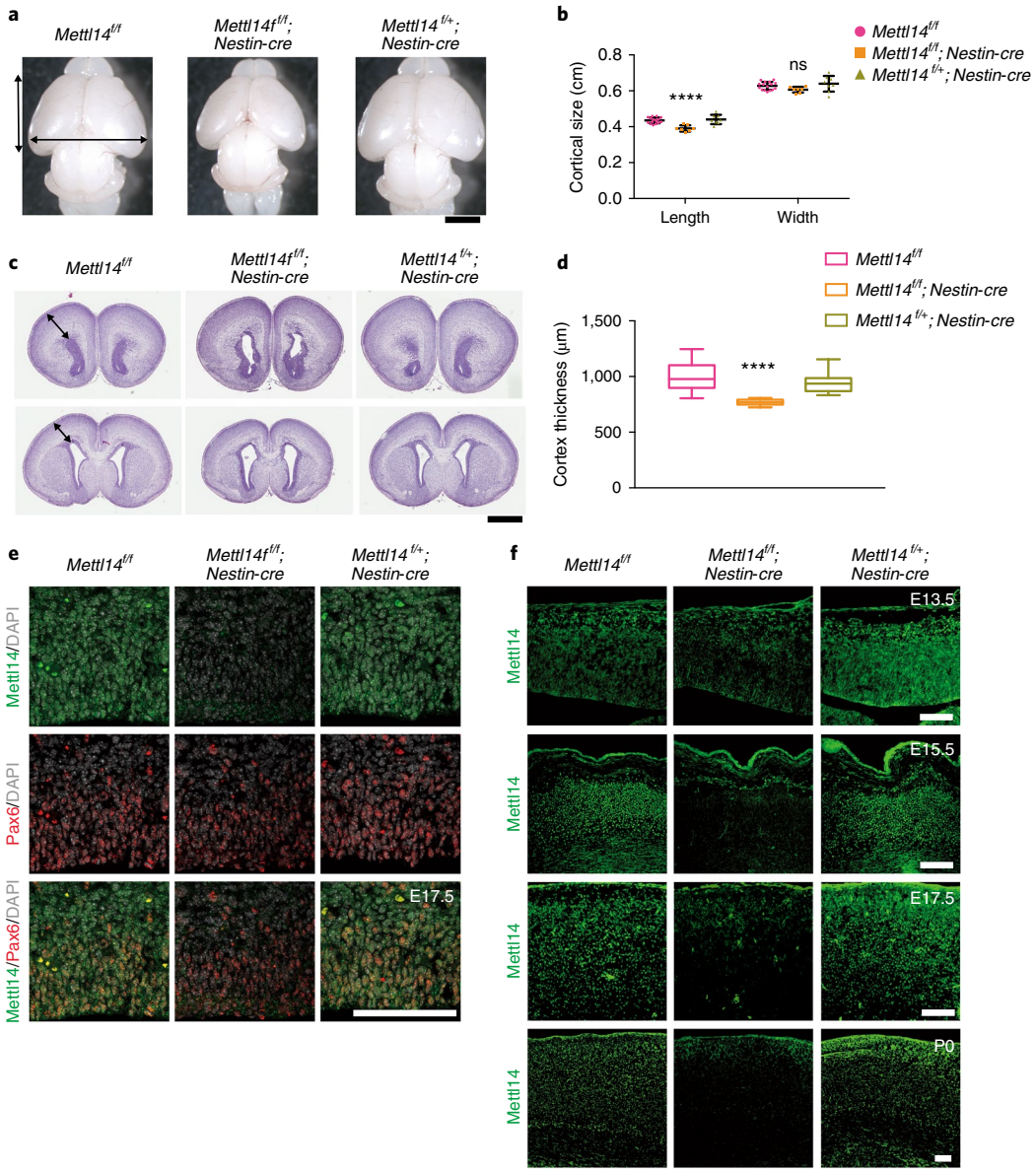

Fig. 1 | *Mettl14* regulates the size of mouse cerebral cortex. a, Representative images of whole brains from *Mettl14*$^{f/f}$ (wild-type (WT); left), *Mettl14*$^{f/f}$;*Nestin-cre* (KO; middle) and *Mettl14*$^{f/+}$;*Nestin-cre* (heterozygous (Het); right) mice pups at P0; black arrows indicate cortex length and width. Scale bar represents 2 mm. **b**, Quantification of cortical length and width at P0; one-way ANOVA (WT: $n=16$; KO: $n=7$,; Het: $n=8$ P0 brains; length, $P=2.559\times10^{-5}$, $F(2, 28)=15.79$; width, $P=0.0869$, $F(2, 28)=2.669$) followed by Bonferroni's post hoc test (length, WT versus KO, $P=4.358\times10^{-5}$, 95% confidence interval (C.I.) = 0.02383–0.06534, WT versus Het, $P=0.9999$, 95% C.I. = −0.02521–0.01446; width, WT versus KO, $P=0.2141$, 95% C.I. = −0.008986–0.05154, WT versus Het, $P=0.6633$, 95% C.I. = −0.04098–0.01686). **c**, Representative images of coronal sections of P0 brains stained with H&E; black arrows indicate cortical thickness. Section shown in upper panel is from the same brain as the one below, but ~1,800 μm anterior to it. Scale bar represents 1 mm. **d**, Quantification of H&E staining, one-way ANOVA ($n=26$ brain sections for all experimental groups; $P=2.9\times10^{-14}$, $F(2, 75)=48.61$) followed by Bonferroni's post hoc test (WT versus KO, $P=4.9\times10^{-14}$, 95% C.I. = 170.1–279.4, WT versus Het, $P=0.0678$, 95% C.I. = −3.027–106.2). **e**, Coronal sections of E17.5 brains stained with antibodies against Mettl14 and Pax6. Similar results were obtained from three independent experiments. **f**, Coronal sections of E13.5, E15.5, E17.5 and P0 brains stained with anti-Mettl14. Similar results were obtained from three independent experiments. Scale bars represent 100 μm. Graphs represent the mean ± s.d. Dots represent data from individual data points. The horizontal lines in the box plots indicate medians, the box limits indicate first and third quantiles, and the vertical whisker lines indicate minimum and maximum values. ns, non-significant. ****$P < 0.0001$.

combined genotyping results from all three stages (Supplementary Table 2). But most *Mettl14*$^{-/-}$ embryos were dead and many had regressed (Supplementary Fig. 1e), indicating that *Mettl14* activity is required for early embryogenesis, a phenotype similar to that of global *Mettl3*-KO mice[13]. Of seven *Mettl14*$^{-/-}$ embryos identified at either E7.5 or E8.5, four were male and three were female, suggesting that phenotypes were not gender specific (Supplementary Fig. 1f).

We then assessed the potential effects of *Mettl14* deletion in NSCs. To do so, we crossed *Mettl14*$^{f/f}$ mice with a *Nestin-Cre* transgenic line to generate *Mettl14*$^{f/f}$;*Nestin-Cre* (*Mettl14*-cKO) mice and littermate controls, including *Mettl14*$^{f/+}$;*Nestin-cre*(heterozygous) and *Mettl14*$^{f/f}$ (non-deleted) mice. Newborn pups were alive and showed no overt morphologic phenotypes (Supplementary Fig. 1g) and normal body weight (Supplementary Fig. 1h). However,

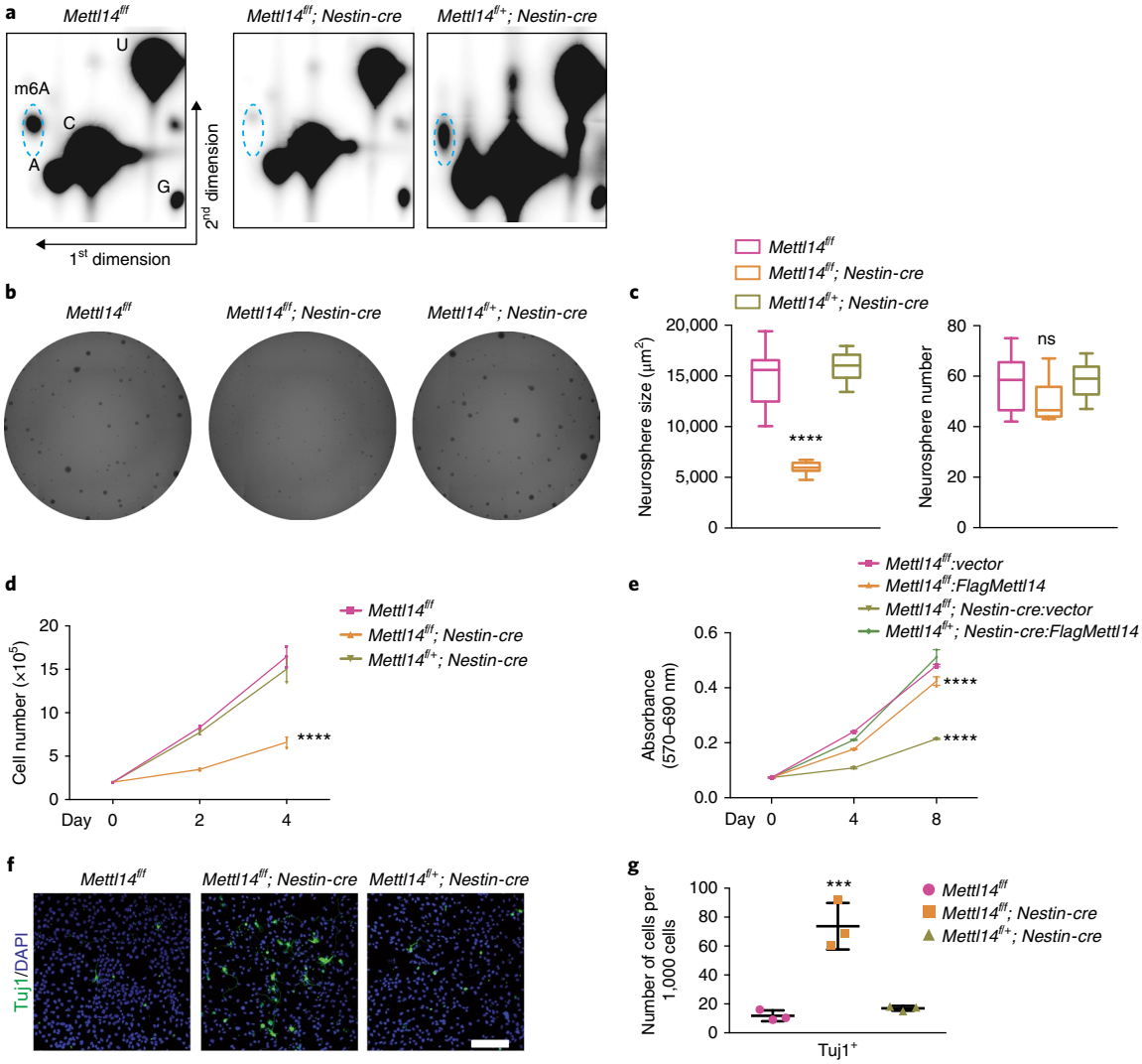

Fig. 2 | *Mettl14* regulates self-renewal of cortical NSCs from E14.5 brain in neurosphere culture. a, Two-dimensional thin-layer chromatography (2D-TLC) analysis of m^{6}A levels in ribosome-depleted (Ribo-) PolyA RNAs isolated from E14.5 NSCs after 7 d of neurosphere culture. Dashed blue circles indicate m^{6}A spots. Similar results were obtained from three independent experiments. **b**, Representative images of neurospheres formed from isolated E14.5 NSCs. **c**, Quantification of neurosphere number and area, one-way ANOVA ($n=12$ cell cultures for all experimental groups; area, $P=9.15\times10^{-13}$, $F(2, 33)=80.21$; number, $P=0.0313$, $F(2, 33)=3.853$) followed by Bonferroni's post hoc test (area, WT versus KO, $P=3.2475\times10^{-11}$, 95% C.I. = 6,781–10,737, WT versus Het, $P=0.2855$, 95% C.I. = −2,999–663.1; number, WT versus KO, $P=0.0724$, 95% C.I. = −0.5596–15.39, WT versus Het, $P=0.9999$, 95% C.I. = = −9.31–6.643). **d**, NSC growth curve. NSCs were plated at 200,000 cells per well in six-well plates and counted 2 and 4 d later; two-way ANOVA ($n=3$ cell cultures for all experimental groups; $P=8.644\times10^{-12}$, $F(2, 18)=143.6$) followed by Bonferroni's post hoc test (WT versus KO, $P=1.2905\times10^{-11}$, 95% C.I. = 4.133–5.666, WT versus Het, $P=0.091$, 95% C.I. = −0.09277–1.44). **e**, Growth curve of *Mettl14*-KO and nondeleted control NSCs transduced with indicated vectors. NSCs were plated in 96-well plates, and numbers were determined by MTT assay; two-way ANOVA ($n=3$ cell cultures for all experimental groups; $P=1.413\times10^{-20}$, $F(3, 24)=396.9$) followed by Bonferroni's post hoc test (WT-vector versus WT-FlagMettl14, $P=1.162\times10^{-8}$, 95% C.I. = 0.02849–0.0514; WT-vector versus KO-vector, $P=1.7709\times10^{-20}$, 95% C.I. = 0.1213–0.1442; WT-vector versus KO-FlagMettl14, $P=0.9999$, 95% C.I. = −0.01183–0.01107). **f**, Immunostaining for anti-Tuj1 in NSCs cultured 7 d in vitro. Scale bar represents 100 μm. **g**, Quantification of immunostaining, one-way ANOVA ($n=3$ fields for all experimental groups; $P=0.0004$, $F(2, 6)=38.49$) followed by Bonferroni's post hoc test (WT versus KO, $P=0.0004$, 95% C.I. = −85.13 to −38.65; WT versus Het, $P=0.9999$, 95% C.I. = −28.37–18.11). Graphs represent the mean ± s.d. Dots represent data from individual data points. The horizontal lines in the box plots indicate medians, the box limits indicate first and third quantiles, and the vertical whisker lines indicate minimum and maximum values. ns, non-significant. ***$P < 0.001$, ****$P < 0.0001$.

all *Mettl14*-cKO mice were dead within the first neonatal week (Supplementary Fig. 1i). When we examined the brains of postnatal day 0 (P0) *Mettl14*-cKO pups, we observed no anomalies in gross anatomy, but we found moderately reduced cortical length (Fig. 1a,b). Hematoxylin and eosin (H&E) staining of coronal sections of P0 mouse brain revealed enlargement of the ventricle and a 23% decrease in cortical thickness in *Mettl14*-cKO brains relative to littermate *Mettl14*$^{f/f}$ controls (Fig. 1c,d). We next examined Mettl14 expression in RGCs by carrying out Mettl14 and Pax6 co-immunostaining on coronal sections of E17.5 brain from nondeleted, cKO and heterozygous mice. Mettl14 was readily detectible in Pax6$^+$ cells in the cortex of nondeleted and heterozygous controls, but not in cKO mice (Fig. 1e). Together, these results suggest that *Mettl14* is required for normal function of NSCs that serve as cortical progenitors.

Next, we evaluated m^{6}A function in isolated embryonic NSCs cultured in vitro. To determine which embryonic stages are appropriate

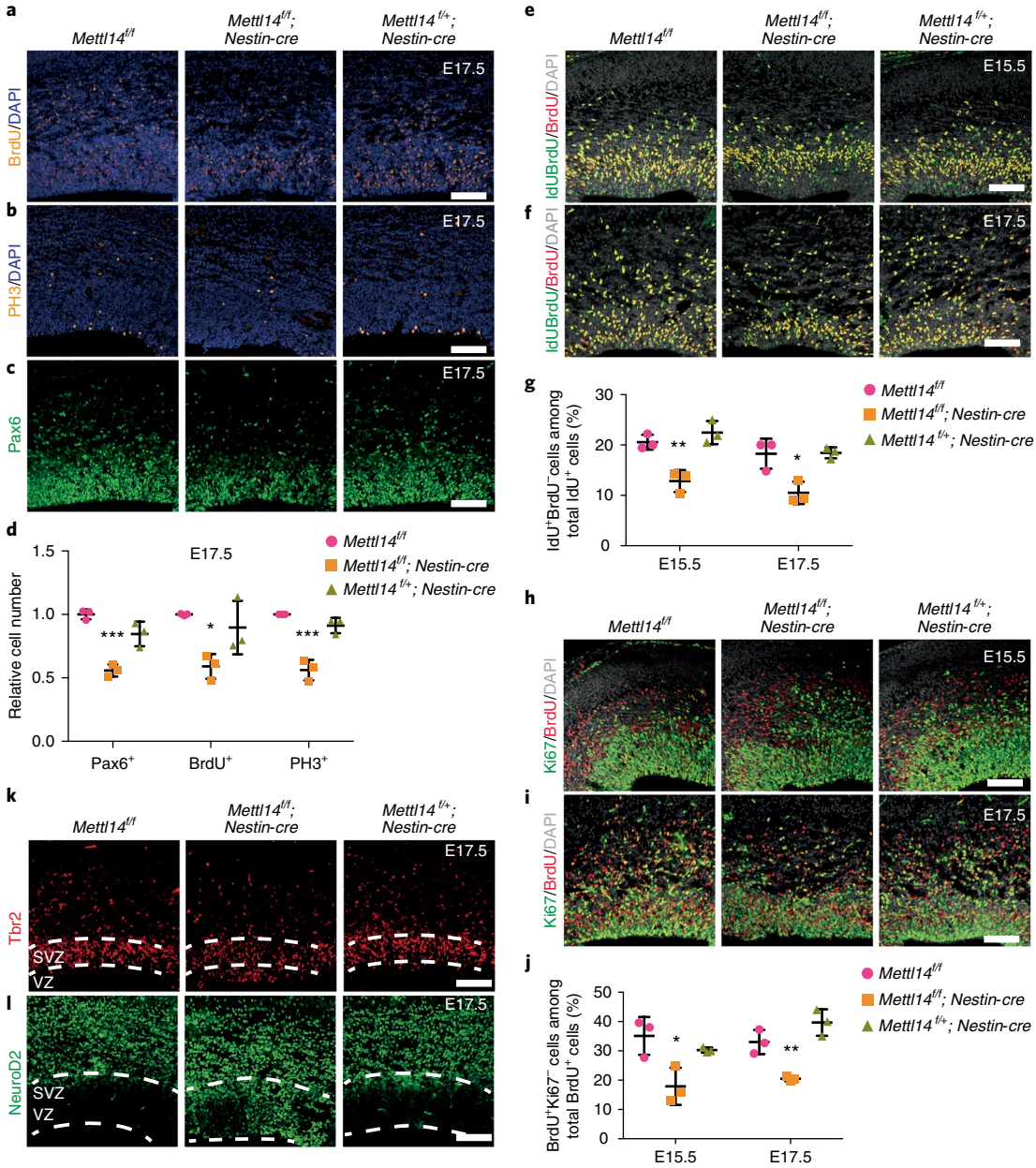

Fig. 3 | *Mettl14* knockout decreases RGC proliferation in vivo. a–c, Coronal sections of E17.5 brains stained with antibodies recognizing BrdU, PH3 and Pax6. Pregnant mothers received a BrdU pulse 30 min before embryo collection. **d**, Quantification of immunostaining from E17.5 sections. Numbers of Pax6$^+$, BrdU$^+$ and PH3$^+$ cells were determined and normalized to those in comparable sections from nondeleted mice; one-way ANOVA ($n=3$ brain sections for all experimental groups; Pax6$^+$, $P=0.0005$, $F(2, 6)=34.41$; BrdU$^+$, $P=0.0231$, $F(2, 6)=7.531$; PH3$^+$, $P=0.0002$, $F(2, 6)=47.73$) followed by Bonferroni's post hoc test (Pax6$^+$, WT versus KO, $P=0.0004$, 95% C.I. = 0.2814–0.6025, WT versus Het, $P=0.0584$, 95% C.I. = –0.006443–0.3146; BrdU$^+$, WT versus KO, $P=0.0194$, 95% C.I. = 0.08378–0.7348, WT versus Het, $P=0.7612$, 95% C.I. = –0.2218–0.4292; PH3$^+$, WT versus KO, $P=0.0002$, 95% C.I. = 0.2976–0.5796, WT versus Het, $P=0.2287$, 95% C.I. = –0.05332–0.2288). **e**,**f**, Coronal sections of E15.5 (**e**) and E17.5 (**f**) brains stained with both anti-BrdU that recognizes BrdU only and anti-IdU that also recognizes BrdU. Pregnant mothers received one IdU injection, followed by one BrdU injection 1.5 h later. After another 0.5 h, the embryonic brains were collected for analysis. **g**, Quantification of the percentage of IdU$^+$BrdU$^-$ cells, representing cells that left S-phase during the 1.5-h chase, among total IdU$^+$ cells. One-way ANOVA ($n=3$ brain sections for all experimental groups; E15.5, $P=0.0025$, $F(2, 6)=19.21$; E17.5, $P=0.0075$, $F(2, 6)=12.35$) followed by Bonferroni's post hoc test (E15.5, WT versus KO, $P=0.0067$, 95% C.I. = 2.835–12.6, WT versus Het, $P=0.5802$, 95% C.I. = –6.787–2.973; E17.5, WT versus KO, $P=0.0107$, 95% C.I. = 2.347–13.19, WT versus Het, $P=0.9999$, 95% C.I. = –5.598–5.244). **h**,**i**, Coronal sections of E15.5 (**h**) and E17.5 (**i**) brains stained with antibodies recognizing Ki67 and BrdU. Pregnant mothers received one BrdU injection 24 h before embryo collection. **j**, Quantification of the percentage of BrdU$^+$Ki67$^-$ cells, representing cells that exited the cell cycle during 24 h, among total BrdU$^+$ cells. One-way ANOVA ($n=3$ brain sections for all experimental groups; E15.5, $P=0.0173$, $F(2, 6)=8.589$; E17.5, $P=0.0016$, $F(2, 6)=22.51$) followed by Bonferroni's post hoc test (E15.5, WT versus KO, $P=0.014$, 95% C.I. = 4.493–29.92, WT versus Het, $P=0.6051$, 95% C.I. = –7.885–17.54; E17.5, WT versus KO, $P=0.01$, 95% C.I. = 3.932–21.2, WT versus Het, $P=0.1249$, 95% C.I. = –15.28–1.99). **k**,**l**, Immunostaining of coronal sections of E17.5 brain with antibodies to the intermediate progenitor marker Tbr2 and the proneural marker Neurod2. Dashed white lines indicate border of VZ/SVZ area. Similar results were obtained from three independent experiments. Scale bars represent 100 μm. Graphs represent the mean ± s.d. Dots represent data from individual data points. ns, non-significant. *$P < 0.05$, **$P < 0.01$, ***$P < 0.001$.

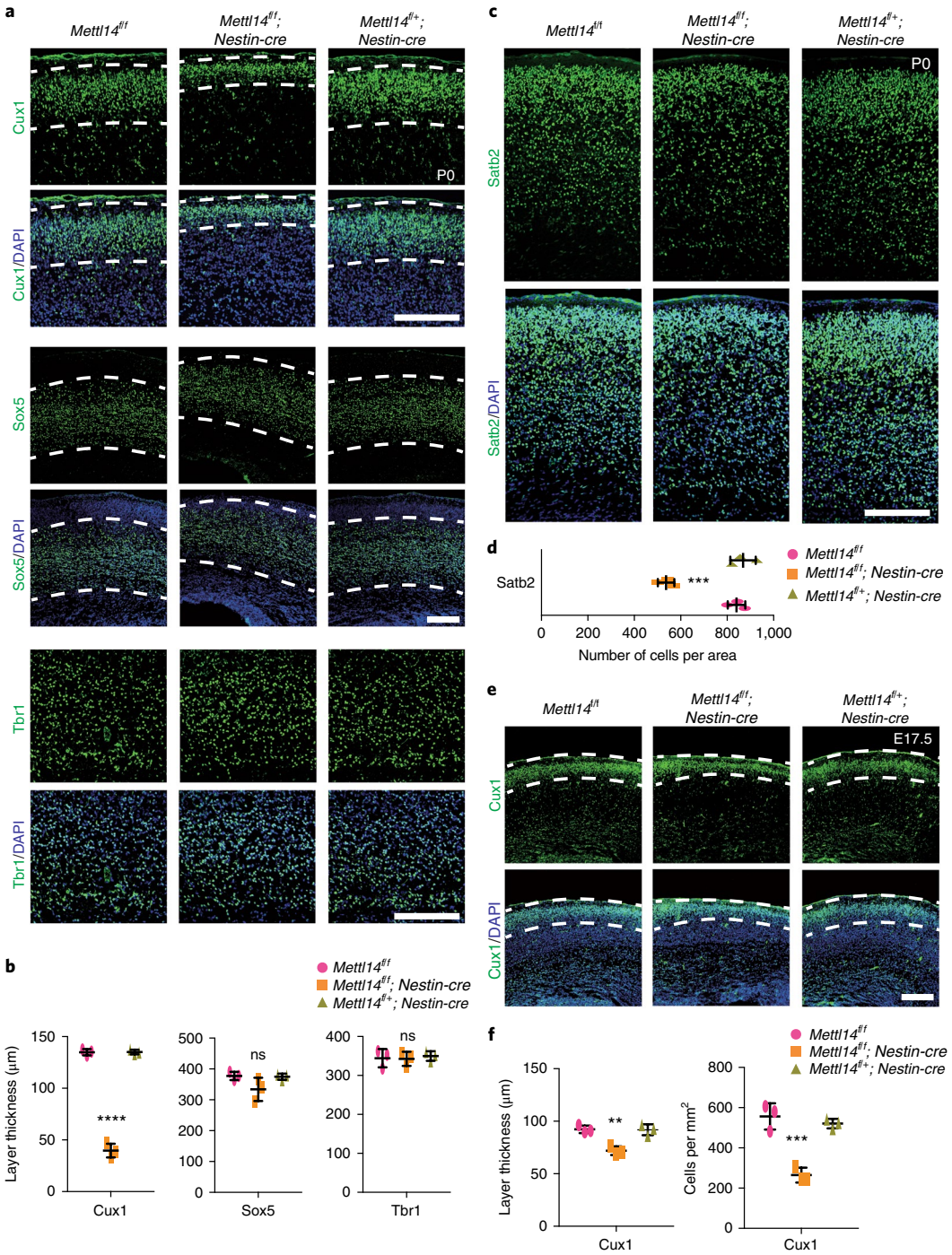

Fig. 4 | *Mettl14* knockout decreases the number of late-born neurons. a, Coronal sections of P0 brains stained for the layer II–IV marker Cux1, the layer V marker Sox5 and the layer VI/subplate (SP) marker Tbr1. Dashed white lines mark borders of Cux1$^+$ and Sox5$^+$ neuronal layers. **b**, Quantification of thickness of Cux1$^+$, Sox5$^+$ and Tbr1$^+$ neuronal layers; one-way ANOVA ($n = 3$ brain sections for all experimental groups; Cux1$^+$, $P = 2.689 \times 10^{-7}$, $F(2, 6) = 461.8$; Sox5$^+$, $P = 0.115$, $F(2, 6) = 3.169$; Tbr1$^+$, $P = 0.8865$, $F(2, 6) = 0.1229$) followed by Bonferroni's post hoc test (Cux1$^+$, WT versus KO, $P = 4 \times 10^{-7}$, 95% C.I. = 84.39–105.9, WT versus Het, $P = 0.9999$, 95% C.I. = −10.97–10.52; Sox5$^+$, WT versus KO, $P = 0.1329$, 95% C.I. = −14.18–101.2, WT versus Het, $P = 0.9999$, 95% C.I. = −55.32–60.06; Tbr1$^+$, WT versus KO, $P = 0.9999$, 95% C.I. = −43.31–46.59, WT versus Het, $P = 0.9999$, 95% C.I. = −50.47–39.42). **c**, Coronal sections of P0 brains stained for the layer II–IV marker Satb2. **d**, Quantification of the number of Satb2$^+$ cells; one-way ANOVA ($n = 3$ brain sections for all experimental groups; $P = 0.00015$, $F(2, 6) = 53.83$) followed by Bonferroni's post hoc test (WT versus KO, $P = 0.0003$, 95% C.I. = 198.2–408.5; WT versus Het, $P = 0.9186$, 95% C.I. = −133.1–77.14). **e**, Coronal sections of E17.5 brains stained for Cux1; dashed white lines mark the border of the Cux1$^+$ neuronal layer. **f**, Quantification of Cux1$^+$ layer thickness within dashed white lines and of the average number of newly generated Cux1$^+$ cells within 1 mm^2, as measured from the VZ to the lower dashed white lines, at E17.5. One-way ANOVA ($n = 3$ brain sections for all experimental groups; thickness, $P = 0.0019$, $F(2, 6) = 21.36$; number, $P = 0.0004$, $F(2, 6) = 36.75$) followed by Bonferroni's post hoc test (thickness, WT versus KO, $P = 0.0025$, 95% C.I. = 9.765–30.85, WT versus Het, $P = 0.9999$, 95% C.I. = −10.13–10.96; number, WT versus KO, $P = 0.0004$, 95% C.I. = 181.5–401.9, WT versus Het, $P = 0.7499$, 95% C.I. = −74.64–145.8). Scale bars represent 200 μm. Graphs represent the mean ± s.d. Dots represent data from individual data points. ns, non-significant. $^{**}P < 0.01$, $^{***}P < 0.001$, $^{****}P < 0.0001$.

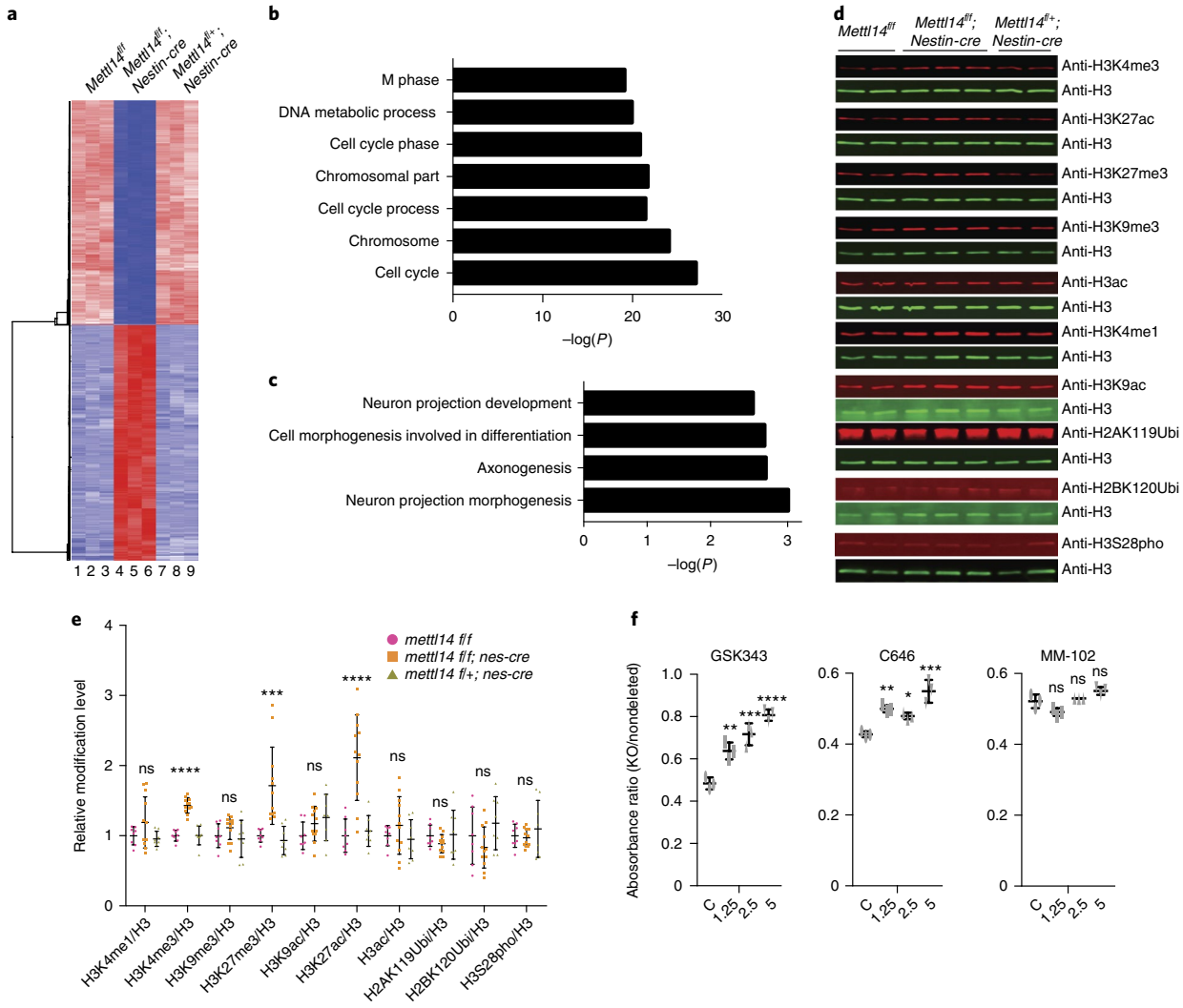

Fig. 5 | m^{6}A regulates NSC gene expression through histone modifications. a, Heat map analysis based on RNA-seq analysis in *Mettl14*-KO versus nondeleted control NSCs. **b**,**c**, GO analysis of genes down- and upregulated in *Mettl14*-KO versus nondeleted control E14.5 NSCs. GO analyses were performed by DAVID. Differentially expressed genes had an adjusted $P < 0.01$ and a twofold or greater expression difference. Among differentially expressed genes, 1,099 are upregulated and 1,487 are downregulated. Numbers of gene counts and exact *P* values for each GO term are listed in Supplementary Fig. 4a. **d**, Representative western blots of acid-extracted histones from E14.5 NSCs using antibodies recognizing H3K4me1, H3K4me3, H3K27me3, H3K9me3, H3K27ac, H3K9ac, H3ac, H2AK119Ubi, H2BK120Ubi and H3S28pho. The band sizes range from 17 to 23 kDa as expected for modified histones. For uncropped images, see Supplementary Fig. 6a. **e**, Quantitation of western blots from E14.5 and E17.5 NSCs. One-way ANOVA ($n = 8$ (WT), 12 (KO), or 8 (Het) independent NSC cultures; H3K4me1, $P = 0.1123$, $F(2, 25) = 2.39$; H3K4me3, $P = 1.06442 \times 10^{-9}$, $F(2, 25) = 52.77$; H3K9me3, $P = 0.2096$, $F(2, 25) = 1.664$; H3K27me3, $P = 0.00013$, $F(2, 25) = 13.07$; H3K9ac, $P = 0.1461$, $F(2, 25) = 2.08$; H3K27ac, $P = 4.796 \times 10^{-6}$, $F(2, 25) = 20.8$; H3ac, $P = 0.3676$, $F(2, 25) = 1.042$; H2AK119Ubi, $P = 0.3592$, $F(2, 25) = 1.067$; H2BK120Ubi, $P = 0.1192$, $F(2, 25) = 2.319$; H3S28pho, $P = 0.5347$, $F(2, 25) = 0.642$) followed by Bonferroni's post hoc test (H3K4me1, WT versus KO, $P = 0.2376$, 95% C.I. = -0.4713–0.09065, WT versus Het, $P = 0.9999$, 95% C.I. = -0.2629–0.3527; H3K4me3, WT versus KO, $P = 1.157 \times 10^{-8}$, 95% C.I. = -0.5518 to -0.3128, WT versus Het, $P = 0.9999$, 95% C.I. = -0.134–0.1278; H3K9me3, WT versus KO, $P = 0.4574$, 95% C.I. = -0.3314–0.1054, WT versus Het, $P = 0.9999$, 95% C.I. = -0.1942–0.2842; H3K27me3, WT versus KO, $P = 0.0008$, 95% C.I. = -1.131 to -0.2956, WT versus Het, $P = 0.9999$, 95% C.I. = -0.3891–0.5256; H3K9ac, WT versus KO, $P = 0.321$, 95% C.I. = -0.4577–0.1121, WT versus Het, $P = 0.1141$, 95% C.I. = -0.5732–0.05098; H3K27ac, WT versus KO, $P = 1.769 \times 10^{-5}$, 95% C.I. = -1.591 to -0.6358, WT versus Het, $P = 0.9999$, 95% C.I. = -0.5908–0.4556; H3ac, WT versus KO, $P = 0.6463$, 95% C.I. = -0.4945–0.2007, WT versus Het, $P = 0.9999$, 95% C.I. = -0.3309–0.4307; H2AK119Ubi, WT versus KO, $P = 0.5288$, 95% C.I. = -0.1242–0.3523, WT versus Het, $P = 0.9999$, 95% C.I. = -0.2759–0.2459; H2BK120Ubi, WT versus KO, $P = 0.6171$, 95% C.I. = -0.2165–0.5511, WT versus Het, $P = 0.6457$, 95% C.I. = -0.5982–0.2426; H3S28pho, WT versus KO, $P = 0.9999$, 95% C.I. = -0.2407–0.2961, WT versus Het, $P = 0.8731$, 95% C.I. = -0.3915–0.1965). **f**, Cell growth analysis based on an MTT assay of NSCs treated with vehicle/DMSO or the MLL1 inhibitor MM-102, the CBP/P300 inhibitor C646, or the Ezh2 inhibitor GSK343. Shown is the absorbance ratio of KO to nondeleted controls at each drug dose. One-way ANOVA ($n = 3$ independent experiments for all experimental groups; GSK343, $P = 4.232 \times 10^{-5}$, $F(3, 8) = 38.47$; C646, $P = 0.0003$, $F(3, 8) = 23.43$; MM-102, $P = 0.0025$, $F(3, 8) = 11.91$) followed by Bonferroni's post hoc test (GSK343, c versus 1.25, $P = 0.0035$, 95% C.I. = -0.2477 to -0.05943, c versus 2.5, $P = 0.0002$, 95% C.I. = -0.3265 to -0.1383, c versus 5, $P = 1.979 \times 10^{-5}$, 95% C.I. = -0.4169 to -0.2287; C646, c versus 1.25, $P = 0.0036$, 95% C.I. = -0.1158 to -0.02744, c versus 2.5, $P = 0.0236$, 95% C.I. = -0.09574 to -0.007344, c versus 5, $P = 0.000103$, 95% C.I. = -0.1654 to -0.07702; MM-102, c versus 0.0625, $P = 0.0507$, 95% C.I. = -8.591×10^{-5} to 0.06086, c versus 1.25, $P = 0.9999$, 95% C.I. = -0.03858–0.02237, c versus 2.5, $P = 0.0615$, 95% C.I. = -0.05958–0.001368). Graphs represent the mean ± s.d. Dots represent data from individual data points. ns, non-significant. *$P < 0.05$, **$P < 0.01$, ***$P < 0.001$, ****$P < 0.0001$.

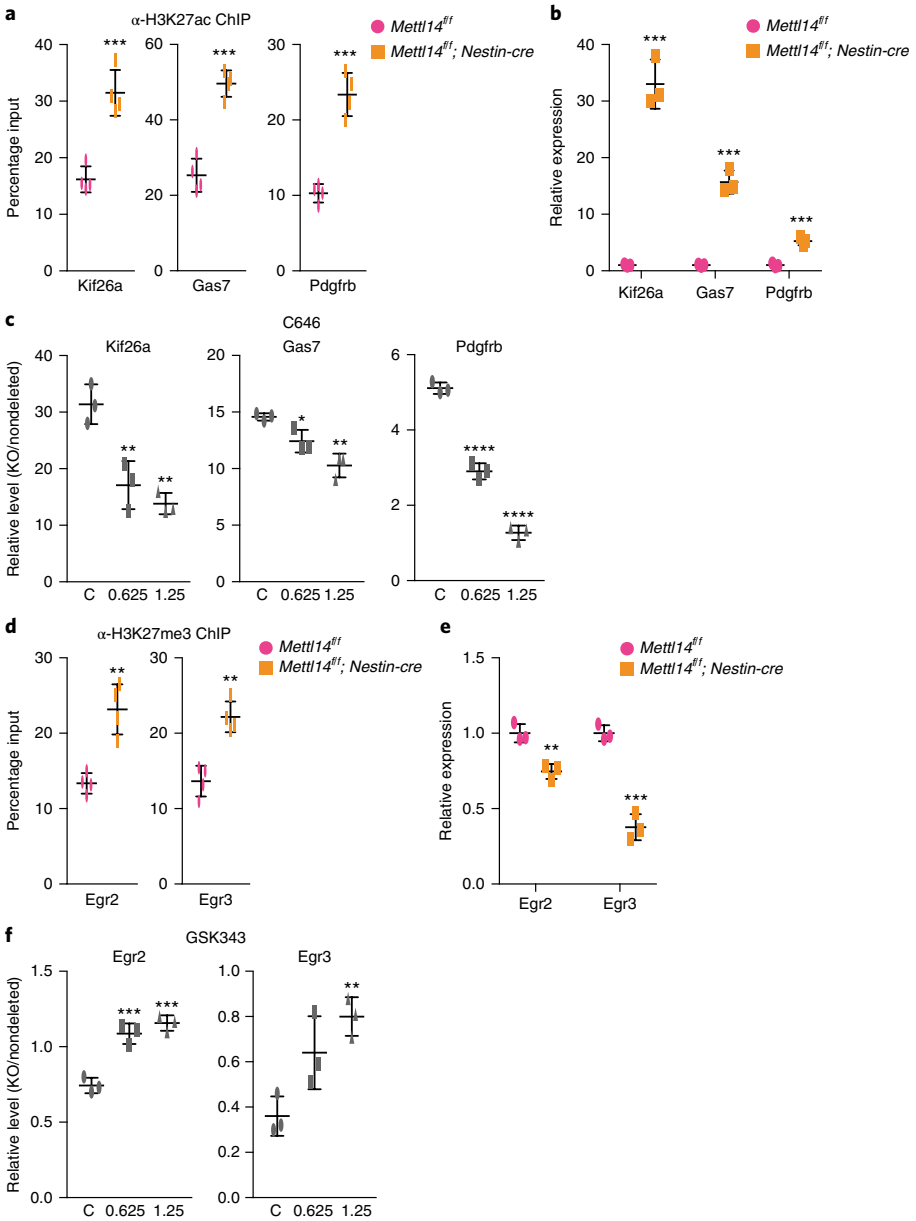

Fig. 6 | H3K27ac inhibitor C646 and H3K27me3 inhibitor GSK343 rescue aberrant gene expression in KO versus nondeleted NSCs. a, H3K27ac ChIP-qPCR showing increased promoter and enhancer H3K27ac of *Kif26a*, *Gas7* and *Pdgfrb* genes in E14.5 *Mettl14*-KO versus nondeleted NSCs. $n = 4$ independent experiments for all experimental groups; two-tailed unpaired *t*-test (Kif26a, $P = 0.0006$, $t = 6.568$, df = 6, 95% C.I. = 9.594–20.99; Gas7, $P = 0.00013$, $t = 8.638$, df = 6, 95% C.I. = 17.41–31.16; Pdgfrb, $P = 0.0002$, $t = 8.395$, df = 6, 95% C.I. = 9.27–16.9). **b**, RT-qPCR showing increased expression of *Kif26a*, *Gas7* and *Pdgfrb* genes in E14.5 *Mettl14*-KO versus nondeleted NSCs. $n = 3$ independent experiments for all experimental groups; two-tailed unpaired *t*-test (Kif26a, $P = 0.0002$, $t = 12.71$, df = 4, 95% C.I. = 25.01–38.99; Gas7, $P = 0.0002$, $t = 12.46$, df = 4, 95% C.I. = 11.41–17.95; Pdgfrb, $P = 0.0008$, $t = 9.08$, df = 4, 95% C.I. = 2.957–5.563). **c**, RT-qPCR showing decreased expression of *Kif26a*, *Gas7* and *Pdgfrb* genes in E14.5 *Mettl14*-KO versus nondeleted NSCs treated with H3K27ac inhibitor C646. One-way ANOVA ($n = 3$ independent experiments for all experimental groups; Kif26a, $P = 0.0015$, $F(2, 6) = 23.04$; Gas7, $P = 0.0027$, $F(2, 6) = 18.67$; Pdgfrb, $P = 8.449 \times 10^{-7}$, $F(2, 6) = 314.3$) followed by Bonferroni's post hoc test (Kif26a, c versus 0.625, $P = 0.0041$, 95% C.I. = 6.126–22.47, c versus 1.25, $P = 0.0014$, 95% C.I. = 9.393–25.73; Gas7, c versus 0.625, $P = 0.045$, 95% C.I. = 0.05735–4.229, c versus 1.25, $P = 0.0018$, 95% C.I. = 2.207–6.379; Pdgfrb, c versus 0.625, $P = 1.431 \times 10^{-5}$, 95% C.I. = 1.75–2.663, c versus 1.25, $P = 5.418 \times 10^{-7}$, 95% C.I. = 3.384–4.296). **d**, H3K27me3 ChIP-qPCR showing increased H3K27me3 at promoters of *Egr2* and *Egr3* genes in E14.5 *Mettl14*-KO versus nondeleted NSCs. $n = 4$ independent experiments for all experimental groups; two-tailed unpaired *t*-test (Egr2, $P = 0.0016$, $t = 5.463$, df = 6, 95% C.I. = 5.412–14.19; Egr3, $P = 0.0010$, $t = 5.928$, df = 6, 95% C.I. = 5.007–12.05). **e**, RT-qPCR showing decreased expression of *Egr2* and *Egr3* genes in E14.5 *Mettl14*-KO versus nondeleted NSCs. $n = 3$ independent experiments for all experimental groups; two-tailed unpaired *t*-test (Egr2, $P = 0.0052$, $t = 5.603$, df = 4, 95% C.I. = −0.3789 to −0.1278; Egr3, $P = 0.0009$, $t = 10.67$, df = 4, 95% C.I. = −0.7855 to −0.4612). **f**, RT-qPCR showing increased expression of *Egr2* and *Egr3* genes in E14.5 *Mettl14*-KO versus nondeleted NSCs treated with H3K27me3 inhibitor GSK343. One-way ANOVA ($n = 3$ independent experiments for all experimental groups; Egr2, $P = 0.0003$, $F(2, 6) = 44.49$; Egr3, $P = 0.01$, $F(2, 6) = 10.94$) followed by Bonferroni's post hoc test (Egr2, c versus 0.625, $P = 0.0007$, 95% C.I. = −0.4826 to −0.2041, c versus 1.25, $P = 0.0002$, 95% C.I. = −0.5526 to −0.2741; Egr3, c versus 0.625, $P = 0.0519$, 95% C.I. = −0.5627–0.002676, c versus 1.25, $P = 0.0072$, 95% C.I. = −0.7227 to −0.1573). Graphs represent the mean ± s.d. Dots represent data from individual data points. ns, non-significant. $^*P < 0.05$, $^{**}P < 0.01$, $^{***}P < 0.001$, $^{****}P < 0.0001$.

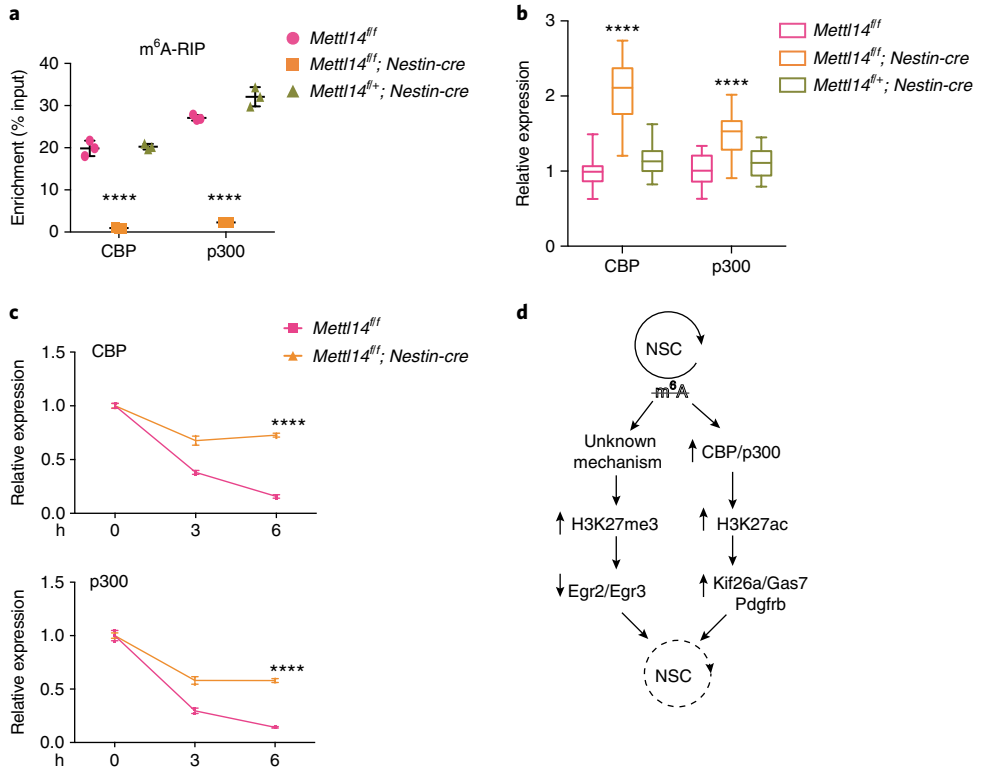

Fig. 7 | m^{6}A regulates mRNA stability of CBP and p300. a, m^{6}A-meRIP-qPCR of CBP and p300 in *Mettl14*-KO versus control E14.5 NSCs. One-way ANOVA ($n=3$ independent experiments for all experimental groups; CBP, $P=1.08\times10^{-6}$, $F(2, 6)=289.4$; p300, $P=3.961\times10^{-7}$, $F(2, 6)=405.5$) followed by Bonferroni's post hoc test (CBP, WT versus KO, $P=1.697\times10^{-6}$, 95% C.I. = 16.18–21.63, WT versus Het, $P=0.9999$, 95% C.I. = −3.13–2.316; p300, WT versus KO, $P=1.113\times10^{-6}$, 95% C.I. = 21.47–28.12, WT versus Het, $P=0.0086$, 95% C.I. = −8.32 to −1.667). **b**, RT-qPCR of *CBP* and *p300* transcripts in E14.5 NSCs cultured for 7 d in vitro; one-way ANOVA ($n=21$ (WT), 33 (KO), or 21 (Het) independent experiments for all experimental groups; CBP, $P=2.380\times10^{-21}$, $F(2, 72)=98.64$; p300, $P=2.751\times10^{-9}$, $F(2, 72)=26.24$) followed by Bonferroni's post hoc test (CBP, WT versus KO, $P=1.306\times10^{-19}$, 95% C.I. = −1.252 to −0.8628, WT versus Het, $P=0.3029$, 95% C.I. = −0.3512–0.07886; p300, WT versus KO, $P=5.254\times10^{-9}$, 95% C.I. = −0.6356 to −0.3153, WT versus Het, $P=0.2011$, 95% C.I. = −0.3058–0.04839). **c**, RT-qPCR of *CBP* and *p300* transcripts in ActD-treated E14.5 NSCs. *P* values are generated by two-way ANOVA ($n=3$ independent experiments for all experimental groups; CBP, $P=1.262\times10^{-11}$, $F(1, 12)=602.5$; p300, $P=8.738\times10^{-10}$, $F(1, 12)=291.7$) followed by Bonferroni's post hoc test (CBP, 0 h, $P=0.9999$, 95% C.I. = −0.05658–0.05658, 3 h, $P=1.714\times10^{-8}$, 95% C.I. = −0.3518 to −0.2386, 6 h, $P=7.954\times10^{-12}$, 95% C.I. = −0.6268 to −0.5136; p300, 0 h, $P=0.9999$, 95% C.I. = −0.06777–0.06777, 3 h, $P=1.988\times10^{-7}$, 95% C.I. = −0.3522 to −0.2167, 6 h, $P=1.50564\times10^{-9}$, 95% C.I. = −0.5046 to −0.3691). **d**, A model in which m^{6}A loss alters histone modifications partly through regulation of mRNA stability of histone modifiers, and altered histone modifications aberrantly repress proliferation-related genes and activate differentiation-related genes, resulting in loss of NSC ground state. Graphs represent the mean ± s.d. Dots represent data from individual data points. The horizontal lines in the box plots indicate medians, the box limits indicate first and third quantiles, and the vertical whisker lines indicate minimum and maximum values. ****$P < 0.0001$.

to select Mettl14-deficient NSCs, we examined Mettl14 protein expression in coronal sections prepared from E13.5, E15.5, E17.5 and P0 brains from cKO, heterozygous and nondeleted control mice. Immunostaining revealed residual Mettl14 staining in the cerebral cortex at E13.5 in *Mettl14*-cKO brain, whereas Mettl14 signals in cortex were absent from E15.5 onward (Fig. 1f). Heterozygous mice showed Mettl14 signals comparable to those of nondeleted controls. Thus, for further analysis we chose E14.5 and E17.5 cortical NSCs and cultured them as neurospheres for 7 d before harvesting them for analysis.

We observed comparable phenotypes in subsequent in vitro analysis of E14.5 and E17.5 NSCs. Unless stated otherwise, our results are those of experiments conducted in E14.5 NSCs. Following confirmation of Mettl14 loss in KO NSCs by western blotting (Supplementary Fig. 2a), we assessed m^{6}A levels from E14.5 neurospheres. Thin-layer chromatography (TLC) analysis revealed an almost total loss of m^{6}A in polyA RNA isolated from *Mettl14*-KO versus nondeleted NSCs, whereas heterozygous cells displayed m^{6}A levels comparable to those seen in nondeleted controls (Fig. 2a), suggesting that the KO system that we generated is ideal for studying m^{6}A function in NSCs.

To characterize KO versus control NSCs, we used a Celigo image cytometer and software to image neurospheres and assess their number and size. Although *Mettl14*-KO, heterozygous and nondeleted control NSCs derived from E14.5 embryos formed a similar number of neurospheres, neurosphere size, as reflected by neurosphere area in this system, decreased by ~55% in KO versus nondeleted control cells, whereas neurosphere size from heterozygous cells was comparable to that seen in nondeleted controls (Fig. 2b,c). Consistently, those same *Mettl14*-KO NSCs exhibited significantly decreased proliferation, as determined by cell-counting analysis (Fig. 2d). Similar proliferation defects were detected in NSCs taken from E17.5 *Mettl14*-cKO mice (Supplementary Fig. 2b). Annexin V flow cytometry (Supplementary Fig. 2c,d) and TUNEL (terminal deoxynucleotidyl transferase (TdT) dUTP nick-end labeling) analysis (Supplementary Fig. 2e) of E14.5 NSCs confirmed that the effects were not a result of increased apoptosis. To ensure that proliferation defects were a result of *Mettl14* deletion, we performed

rescue experiments by overexpressing Flag-tagged *Mettl14* in E14.5 KO NSCs. Western and dot blot analysis confirmed *Mettl14* transgene expression (Supplementary Fig. 2f) and the restoration of m^{6}A (Supplementary Fig. 2g). Notably, *Mettl14* overexpression did not increase the proliferation of nondeleted NSC controls (Fig. 2e), but increased the proliferation of *Mettl14*-KO NSCs to rates comparable to that of controls (Fig. 2e). These results suggest that *Mettl14* and concomitant m^{6}A RNA modification regulate NSC proliferation, at least in vitro.

It is well established that decreased NSC proliferation is coupled with premature NSC differentiation[14]. Thus, we checked for the presence of cells expressing the neuronal marker Tuj1 in E14.5 NSCs cultured for 7 d as neurospheres. Immunostaining analysis revealed a 6.2-fold increase in the number of Tuj1$^+$ cells in KO versus control NSCs (Fig. 2f,g), whereas the number of Tuj1$^+$ cells was comparable between heterozygous and nondeleted controls, suggesting that Mettl14 loss leads to premature neuronal differentiation. Together, these results suggest that Mettl14 regulates NSC self-renewal.

To determine whether the loss of an m^{6}A demethylase would have the opposite effect on NSC proliferation, we knocked down two reported m^{6}A demethylases, Fto and Alkbh5[9,15], separately in wild-type NSCs. Reverse-transcription quantitative PCR (RT-qPCR) analysis showed high knockdown efficiency in each case, and western blots revealed a marked decrease in Fto and Alkbh5 protein levels in the respective knockdown cells (Supplementary Fig. 2h,i,k,l). Nonetheless, NSC proliferation in vitro was not altered by the loss of either protein (Supplementary Fig. 2j,m). Some reports suggest that changes in expression of either Fto or Alkbh5 have only moderate effects on m^{6}A levels and that both factors likely regulate m^{6}A modification of a subset of transcripts[15–17]. Our results suggest that mRNAs that function in NSC proliferation are not regulated by either Fto or Alkbh5.

The size of the cortical RGC pool is reduced in *Mettl14*-cKO mouse brain. We next examined the effect of *Mettl14* on the proliferation of primary cortical stem cells or RGCs in vivo. To do so, we determined the number of S-phase cells in the cortex of E13.5, E15.5 or E17.5 *Mettl14*-cKO, heterozygous and nondeleted control embryos by injecting pregnant females with bromodeoxyuridine (BrdU) and harvesting embryos 0.5 h later, which detected only cells undergoing DNA replication at that time point. Immunostaining showed that the number of BrdU$^+$ cells decreased by 19% in E15.5 *Mettl14*-cKO compared with nondeleted control brain (Supplementary Fig. 3a,d), and that number was 40% when analysis was conducted at E17.5 (Fig. 3a,d). Similarly, we also observed a 44% and 45% decrease in the number of cells expressing the mitotic marker phospho-histone H3 (PH3) at the apical membrane of the cortical VZ in cKO versus nondeleted control brain at E15.5 and E17.5, respectively (Supplementary Fig. 3b,d and Fig. 3b,d). To determine the number of RGCs, we assessed brain coronal sections at all three stages with the RGC marker Pax6. Consistently, we detected a 45% decrease in the number of Pax6$^+$ RGCs in the VZ of E17.5 *Mettl14*-cKO brain versus controls (Fig. 3c,d) and a 14% decrease at E15.5 (Supplementary Fig. 3c,d). All experiments showed highly comparable results between heterozygous and nondeleted control RGCs (Fig. 3a–d and Supplementary Fig. 3a–d). We did not detect differences in BrdU, PH3 or Pax6 staining relative to that in nondeleted controls in the cortex of E13.5 *Mettl14*-cKO brains (Supplementary Fig. 3e–g), consistent with the finding that residual *Mettl14* is present in cortex at E13.5 (Fig. 1f). Immunostaining with the apoptosis marker cleaved caspase-3 revealed no change in the number of apoptotic cells in the cortex of E17.5 and E15.5 *Mettl14*-cKO brains relative to nondeleted controls (Supplementary Fig. 3h,i). To understand how Mettl14 loss might affect RGC proliferation, we examined cell cycle progression and cell cycle exit of RGCs from the brains of E15.5 and E17.5 *Mettl14*-cKO versus control mice. We carried out sequential 5-iodo-2′-deoxyuridine (IdU) and BrdU injection to evaluate cell cycle progression, followed by IdU and BrdU double-staining of cortical sections[18]. We then determined the percentage of IdU$^+$BrdU$^-$ cells, which represented the cells that had progressed past S-phase, versus all IdU$^+$ cells, a group that included both proliferating cells and cells that had left S-phase. We detected a 38% and 43% decrease in E15.5 and E17.5 *Mettl14*-cKO embryos, respectively, compared with the nondeleted control, suggesting that Mettl14 loss disrupts normal RGC cell cycle progression (Fig. 3e–g). Heterozygous and nondeleted control RGCs yielded comparable results (Fig. 3e–g). To determine whether Mettl14 loss alters cell cycle exit, we performed BrdU-Ki67 double-staining of cortical sections from the brains of mice pulsed with BrdU and analyzed 24 h later. Mettl14 loss resulted in a 50% and 39% decrease in cells exiting the cell cycle from E15.5 and E17.5 *Mettl14*-cKO embryos, respectively, versus nondeleted controls, suggesting that Mettl14 is required for normal RGC cell cycle exit (Fig. 3h–j). Heterozygous and nondeleted control RGCs yielded comparable results (Fig. 3h–j). Together, these data strongly suggest that Mettl14 regulates the RGC cell cycle and that the RGC pool in cortex is substantially reduced in *Mettl14*-cKO mice.

We then examined RGC premature differentiation in the cortical VZ of E15.5 and E17.5 *Mettl14*-cKO brains using Eomes (Tbr2), a marker of intermediate progenitor cells located at the sub-ventricular zone (SVZ), and the proneural marker Neurod2 (ND2). Notably, patches of ND2$^+$Tbr2$^+$ cells were seen consistently at E15.5 and E17.5 in areas close to the apical surface of the cortical VZ of *Mettl14*-cKO brain, but were absent in comparably staged littermate controls (Supplementary Fig. 3j,k and Fig. 3k,l). Together, these data suggest that *Mettl14* is required to prevent NSC premature differentiation and maintain the NSC pool in vivo.

***Mettl14* deletion results in reduced numbers of late-born neurons.** We next evaluated the effects of *Mettl14* loss on cortical neurogenesis. In P0 mice, neurons differentiated from RGCs are found in six distinct cortical layers containing neuronal subtypes identifiable by specific markers. Thus, we stained coronal sections from cKO and comparably staged littermate controls at P0 for the following markers: Cux1, which is expressed in late-born neurons and is a marker of upper neuronal layers II–IV; Sox5, which is expressed in early-born neurons and is a marker of layer V; and Tbr1, which is expressed in postmitotic neurons and is a marker of layer VI to the subplate. Overall, layer organization was comparable in cKO and control mice. When we assessed layer thickness, the thickness of layers marked by Sox5 and Tbr1 did not differ significantly between genotypes (Fig. 4a,b). However, we observed a 70% decrease in the thickness of Cux1$^+$ layers (II–IV) (Fig. 4a,b). To confirm the loss of neurons from these layers, we stained sections from P0 embryos for a different layer II–IV marker, Satb2, and observed an ~34% decrease in the number of Satb2$^+$e neurons in cKO mice versus littermate controls (Fig. 4c,d). When we examined cortical Cux1 staining at E17.5, we detected a 22% reduction in the thickness of Cux1$^+$ layers and a 50% reduction in the number of newly generated Cux1$^+$ cells residing in a region between the VZ and layer IV in *Mettl14*-cKO mice versus controls (Fig. 4e,f). These results suggest that *Mettl14* loss may deplete the progenitor pool in a way that is reflected by loss of late-born neurons.

***Mettl14* knockout leads to genome-wide changes in histone modification that perturb gene expression.** To assess molecular mechanisms underlying m^{6}A-regulated NSC activity, we cultured NSCs from E14.5 *Mettl14*-cKO, heterozygous and nondeleted control embryos for 7 d and performed RNA sequencing (RNA-seq). *Mettl14*-KO NSCs exhibited distinct gene expression profiles relative to nondeleted and heterozygous controls (which showed comparable profiles; Fig. 5a and Supplementary Table 3).

Gene Ontology analysis (GO) suggested that the most significantly upregulated genes function in NSC differentiation, whereas downregulated genes are associated with cell proliferation (Fig. 5b,c and Supplementary Fig. 4a), changes that are reflective of observed phenotypes. We then evaluated potential mechanisms underlying these changes in gene expression. It is well established that m^{6}A destabilizes transcripts[4,13,19,20]. However, we detected only a weak correlation between m^{6}A loss and increase in transcript abundance (Supplementary Fig. 4b, Supplementary Tables 3 and 4), suggesting that different m^{6}A-related mechanisms modulate mRNA levels. Given that modification of histone tails is a critical mechanism of gene regulation in mammalian cells[21], we asked whether m^{6}A RNA modification may also change histone modifications by performing western blotting on acid-extracted histones from KO versus control NSCs isolated at both E14.5 and E17.5. We evaluated a panel of well-studied histone modifications that have been reported to regulate stem cell activities, including histone H3 phosphorylation, histone H2A and H2B ubiquitination, three types of histone acetylation, and four types of histone methylation[22–33]. These histone marks are associated with either gene activation or repression. Representative western blots of E14.5 NSCs are shown in Fig. 5d. We quantified western blots from E14.5 and E17.5 by calculating the ratios of respective histone modifications to total H3 protein in KO, heterozygous and nondeleted control NSCs. Although we observed no significant change in any of the histone modifications that we tested between heterozygous and nondeleted control samples (Fig. 5d,e), we detected a significant increase in acetylation of histone H3 at lysine 27 (H3K27ac; 111% increase), trimethylation of histone H3 at lysine 4 (H3K4me3; 43% increase) and trimethylation of histone H3 at lysine 27 (H3K27me3; 71% increase) in *Mettl14*-KO NSCs versus nondeleted controls (Fig. 5d,e). These results suggest that m^{6}A regulates specific histone modifications.

To determine whether these changes alter NSC proliferation, we searched for chemical inhibitors that antagonize activities associated with upregulated histone modifications to determine whether inhibitor treatment of E14.5 KO NSCs would rescue cell proliferation defects. Three inhibitors were commercially available: MM102, which inhibits mixed-lineage leukemia (MLL) function and H3K4me3 formation; C646, which inhibits the H3K27 acetyltransferase Crebbp (CBP)/p300 activity; and GSK343, which inhibits Ezh2-dependent H3K27me3 formation. We then seeded comparable numbers of NSCs of all three genotypes, added inhibitor or DMSO vehicle at day 0, and determined cell number via MTT assays 4 d later. After DMSO treatment, the number of KO NSCs was ~50% that of nondeleted controls, reflecting slower proliferation, as anticipated (Fig. 5f). GSK343 treatment at 1.25, 2.5 and 5 μM increased the ratios of KO to nondeleted control NSCs to 64%, 71% and 80%, respectively (Fig. 5f), whereas the percentages of heterozygous to nondeleted control NSCs were unchanged by GSK343 treatment (Supplementary Fig. 4c). These observations suggest that blocking the formation of H3K27me3 rescues the growth defects of KO NSCs. Increased ratios of KO versus nondeleted control NSCs were also seen after C646 treatment (Fig. 5f and Supplementary Fig. 4c), suggesting that blocking of H3K27ac also blocks the proliferation defects of KO NSCs. By contrast, treatment of E14.5 NSCs with MM102 had no effect (Fig. 5f and Supplementary Fig. 4c). These results suggest that m^{6}A regulates NSC proliferation, at least in part, through H3K27me3 and H3K27ac modifications.

H3K27me3 marks gene promoters and is associated with silencing[34,35], whereas H3K27ac, which is enriched at promoters and enhancers, is associated with gene activation[36,37]. Thus, we asked whether increased promoter H3K27me3 was associated with gene downregulation, whereas increased promoter/enhancer H3K27ac was associated with gene upregulation in E14.5 *Mettl14*-KO versus control NSCs. To do so, we performed H3K27me3 and H3K27ac ChIP-seq analysis on E14.5 KO versus nondeleted NSCs (Supplementary Tables 5 and 6) and correlated changes in gene expression with altered histone modification. In total, the intensity of 1,610 promoter/enhancer H3K27ac peaks, defined as peaks within a 10-kb region up- or downstream of a transcriptional start site (TSS), were significantly altered in KO versus control cells. Pearson correlation analysis showed a positive correlation between changes in peak intensity and changes in gene expression ($r=0.06195$, $P=0.01292$) in KO versus control NSCs, suggesting that H3K27ac functions in m^{6}A-regulated gene activation. We also detected 434 altered H3K27me3 promoter peaks, defined as peaks within 2 kb upstream of a TSS, in KO versus control NSCs. Although in this case we did not detect a significant correlation between changes in peak intensity and gene expression ($P=0.05784$) using all 434 genes, we detected a strongly negative Pearson correlation ($r=-0.38804$, $P<0.02$) when we analyzed only downregulated genes ($\log_2$ fold change ≤ -0.6) in KO versus control NSCs, suggesting that H3K27me3 levels are positively correlated to the repression of genes showing decreased expression.

To further assess the relevance of altered H2K27ac and H3K27me3 modifications to NSC gene expression, we asked whether altered transcript abundance seen in KO versus control NSCs could be rescued by treating cells with inhibitors of H2K27ac (C646) or of H3K27me3 (GSK343). Using overlaying ChIP-seq and RNA-seq data and coupling that to Ingenuity pathway analysis (IPA), we picked five differentiation-related genes showing increased H3K27ac and increased expression and five cell-proliferation related genes showing increased H3K27me3 but decreased expression for rescue experiment. Indeed, C646 treatment resulted in significantly decreased expression of the neuritogenesis regulators Kif26a[38], Gas7[39] and Pdgfrb[40], in KO NSCs when compared with that in nondeleted NSCs (Fig. 6a–c), whereas GSK343 treatment increased expression of the transcription factors Egr2 and Egr3, which are known to promote proliferation[41] (Fig. 6d–f). These results suggest that m^{6}A-regulated histone modification functions in NSC gene expression.

m^{6}A regulates the stability of CBP and p300 transcripts. We then asked how m^{6}A might regulate histone modifications. To do so, we first evaluated the presence of m^{6}A on transcripts encoding the H3K27 acetyltransferases CBP and p300 and the polycomb repressive complex (PRC2) subunits Ezh2, Suz12 and Eed, which catalyze H3K27me3, by methylated RNA immunoprecipitation (meRIP). We detected a 20–30% enrichment of m^{6}A over input in *CBP* (*Crebbp*) and *p300* (*Ep300*) mRNAs, which was lost in E14.5 *Mettl14*-KO NSCs (Fig. 7a). In contrast, only a 0.4–0.6% enrichment of m^{6}A was observed in *Ezh2*, *Eed* and *Suz12* mRNAs, and the extremely low levels that we observed for Ezh2 and Eed persisted in KO cells (Supplementary Fig. 5), suggesting that the signals that we detected are a result of the immunoprecipitation background.

We then evaluated potential changes in the stability of *CBP* and *p300* mRNAs. We observed a significant increase in both *CBP* and *p300* mRNA levels in E14.5 *Mettl14*-KO versus control NSCs (Fig. 7b). We then assayed mRNA stability by treating E14.5 cultured KO and control NSCs with actinomycin D (ActD) to block transcription and harvesting cells 3 and 6 h later. Both CBP and p300 showed significantly increased mRNA stability in *Mettl14*-KO NSCs compared with nondeleted control NSCs (Fig. 7c), suggesting that m^{6}A may regulate histone modification by destabilizing transcripts that encode histone modifiers.

Discussion

By conditionally inactivating *Mettl14* in embryonic NSCs, we discovered that Mettl14 is required for NSC proliferation and maintains NSCs in an undifferentiated state (Figs. 1–3). Thus, our findings reveal a previously unknown, but essential, function of m^{6}A RNA methylation in the regulation of NSC self-renewal. We also

observed decreased numbers of late-born neurons, which are generated from RGCs after E15.5, in the cortex of *Mettl14*-cKO animals at E17.5 and P0 (Fig. 4), consistent with the loss of Mettl14 expression and a decrease in size of the RGC pool. Notably, although Mettl14 loss promoted premature NSC differentiation, the identity of neuronal subtypes in each neuronal layer was not obviously affected in cortex of *Mettl14*-cKO brain. Thus, we conclude that RGCs lacking *Mettl14* remain capable of differentiation and migration, and propose that cortical defects seen in *Mettl14*-KO mice are primarily a result of perturbed NSC self-renewal. Overall, our results provide a benchmark to further explore mechanisms underlying perturbed m^{6}A RNA methylation in neurodevelopmental disorders. We also detected Mettl14 expression in postmitotic cortical neurons (Fig. 1e); thus, the possibility of a Mettl14 function in these cells cannot be excluded. However, given that the *Mettl14*-cKO mice in our study died shortly after birth, examination of potential Mettl14 function in neurons at later postnatal or adult stages was not possible. We also note that, although we found a specific reduction in the number of upper layer projection neurons in the cortex of *Mettl14*-cKO versus control mice, we do not exclude the possibility that Mettl14 regulates production of neurons in other cortical layers. Analysis of that effect is likely to require the use of a Cre driver to delete Mettl14 at an earlier time point than E13.5.

Our data suggest, for the first time, to our knowledge, the existence of cross-talk between RNA and histone modification. Although m^{6}A reportedly regulates gene expression through diverse mechanisms such as mRNA stability[4,13,19,20], splicing[15,42–44] and translation[45,46], an interaction between m^{6}A modification and epigenetic mechanisms has not been explored. Thus, our finding that m^{6}A RNA methylation regulates specific histone modifications, including H3K27me3, H3K27ac and H3K4me3, represents a previously unknown mechanism of gene regulation. Among these modifications, H3K27ac and H3K4me3 are associated with gene activation, and H3K27me3e with repression, consistent with our observations that there is no marked bias toward gene activation or repression in *Mettl14*-KO NSCs compared with controls (Fig. 5a). Importantly, our data show that, in *Mettl14*-KO cells, different m^{6}A-regulated histone marks regulate expression of genes of different function (Fig. 6), suggesting that m^{6}A-regulated active and repressive histone modifications work synergistically to ensure an NSC ground state. Synergy is also evident in our observation that treatment of cells with either H3K27me3 or H3K27ac inhibitors can, at least partially, restore cell proliferation in *Mettl14*-KO NSCs (Fig. 5). We did not observe any effects of the H3K4me3 inhibitor MM-102 on NSC proliferation. However, unlike H3K27ac and H3K27me3, which are regulated by distinct enzymes, H3K4me3e modification is catalyzed by a panel of SET domain proteins[47]. Although MM-102 is widely used to test H3K4me3 function, it inhibits the formation of a MLL1–WDR5 complex and therefore targets only the subset of H3K4me3 modifications that are dependent on MLL1[48]. As yet, there are no inhibitors available that inhibit activities of most H3K4me3 methyltransferases and therefore sufficiently abolish H3K4me3. Thus, we cannot exclude the possibility that m^{6}A-regulated H3K4me3 regulates NSC proliferation. Future studies may reveal that m^{6}A regulates levels of histone modifications other than H3K27ac, H3K27me3 and H3K4me3.

We further showed that m^{6}A regulates histone modifications directly by destabilizing transcripts that encode histone modifiers. It is evident that such a mechanism is applicable to the H3K27 acetyltransferase CBP/p300, but not to subunits in the PRC2 complex, suggesting that m^{6}A regulates histone modifications through distinct mechanisms. Identification of those mechanisms warrants future investigation.

In summary, we propose a model (Fig. 7d) in which m^{6}A loss alters histone modifications partly by regulating mRNA stability of histone modifiers, and altered histone modifications aberrantly repress proliferation-related genes and activate differentiation-related genes, resulting in a loss of NSC ground state. Our results provide an in-depth analysis of m^{6}A in brain neural stem cells and suggest that there is an interaction between m^{6}A and histone modification as a mechanism of gene regulation.

Methods

Methods, including statements of data availability and any associated accession codes and references, are available at https://doi.org/10.1038/s41593-017-0057-1.

Received: 4 July 2017; Accepted: 4 December 2017;
Published online: 15 January 2018

References

1. Meyer, K. D. et al. Comprehensive analysis of mRNA methylation reveals enrichment in 3′ UTRs and near stop codons. *Cell* **149**, 1635–1646 (2012).
2. Dominissini, D. et al. Topology of the human and mouse m6A RNA methylomes revealed by m6A-seq. *Nature* **485**, 201–206 (2012).
3. Liu, J. et al. A METTL3-METTL14 complex mediates mammalian nuclear RNA N6-adenosine methylation. *Nat. Chem. Biol.* **10**, 93–95 (2014).
4. Wang, Y. et al. N6-methyladenosine modification destabilizes developmental regulators in embryonic stem cells. *Nat. Cell Biol.* **16**, 191–198 (2014).
5. Sledz, P. & Jinek, M. Structural insights into the molecular mechanism of the m(6)A writer complex. *eLife* **5**, e18434 (2016).
6. Wang, X. et al. Structural basis of N-adenosine methylation by the METTL3-METTL14 complex. *Nature* **534**, 575–578 (2016).
7. Wang, P., Doxtader, K. A. & Nam, Y. Structural basis for cooperative function of Mettl3 and Mettl14 methyltransferases. *Mol. Cell* **63**, 306–317 (2016).
8. Wang, Y. & Zhao, J. C. Update: mechanisms underlying N6-methyladenosine modification of eukaryotic mRNA. *Trends Genet.* **32**, 763–773 (2016).
9. Jia, G. et al. N6-methyladenosine in nuclear RNA is a major substrate of the obesity-associated FTO. *Nat. Chem. Biol.* **7**, 885–887 (2011).
10. Çağlayan, A. O. et al. A patient with a novel homozygous missense mutation in FTO and concomitant nonsense mutation in CETP. *J. Hum. Genet.* **61**, 395–403 (2016).
11. Boissel, S. et al. Loss-of-function mutation in the dioxygenase-encoding FTO gene causes severe growth retardation and multiple malformations. *Am. J. Hum. Genet.* **85**, 106–111 (2009).
12. Hu, W. F., Chahrour, M. H. & Walsh, C. A. The diverse genetic landscape of neurodevelopmental disorders. *Annu. Rev. Genomics Hum. Genet.* **15**, 195–213 (2014).
13. Geula, S. et al. Stem cells. m6A mRNA methylation facilitates resolution of naïve pluripotency toward differentiation. *Science* **347**, 1002–1006 (2015).
14. Hardwick, L. J. & Philpott, A. Nervous decision-making: to divide or differentiate. *Trends Genet.* **30**, 254–261 (2014).
15. Zheng, G. et al. ALKBH5 is a mammalian RNA demethylase that impacts RNA metabolism and mouse fertility. *Mol. Cell* **49**, 18–29 (2013).
16. Hess, M. E. et al. The fat mass and obesity associated gene (Fto) regulates activity of the dopaminergic midbrain circuitry. *Nat. Neurosci.* **16**, 1042–1048 (2013).
17. Mauer, J. et al. Reversible methylation of m6Am in the 5′ cap controls mRNA stability. *Nature* **541**, 371–375 (2017).
18. Martynoga, B., Morrison, H., Price, D. J. & Mason, J. O. Foxg1 is required for specification of ventral telencephalon and region-specific regulation of dorsal telencephalic precursor proliferation and apoptosis. *Dev. Biol.* **283**, 113–127 (2005).
19. Batista, P. J. et al. m(6)A RNA modification controls cell fate transition in mammalian embryonic stem cells. *Cell Stem Cell* **15**, 707–719 (2014).
20. Wang, X. et al. N6-methyladenosine-dependent regulation of messenger RNA stability. *Nature* **505**, 117–120 (2014).
21. Bannister, A. J. & Kouzarides, T. Regulation of chromatin by histone modifications. *Cell Res.* **21**, 381–395 (2011).
22. Avgustinova, A. & Benitah, S. A. Epigenetic control of adult stem cell function. *Nat. Rev. Mol. Cell Biol.* **17**, 643–658 (2016).
23. Castelo-Branco, G. et al. Neural stem cell differentiation is dictated by distinct actions of nuclear receptor corepressors and histone deacetylases. *Stem Cell Rep.* **3**, 502–515 (2014).
24. Qiao, Y., Wang, R., Yang, X., Tang, K. & Jing, N. Dual roles of histone H3 lysine 9 acetylation in human embryonic stem cell pluripotency and neural differentiation. *J. Biol. Chem.* **290**, 2508–2520 (2015).
25. Román-Trufero, M. et al. Maintenance of undifferentiated state and self-renewal of embryonic neural stem cells by Polycomb protein Ring1B. *Stem Cells* **27**, 1559–1570 (2009).
26. Voncken, J. W. et al. Rnf2 (Ring1b) deficiency causes gastrulation arrest and cell cycle inhibition. *Proc. Natl. Acad. Sci. USA* **100**, 2468–2473 (2003).

27. cIshino, Y. et al. Bre1a, a histone H2B ubiquitin ligase, regulates the cell cycle and differentiation of neural precursor cells. *J. Neurosci.* **34**, 3067–3078 (2014).
28. Pereira, J. D. et al. Ezh2, the histone methyltransferase of PRC2, regulates the balance between self-renewal and differentiation in the cerebral cortex. *Proc. Natl. Acad. Sci. USA* **107**, 15957–15962 (2010).
29. Mohn, F. et al. Lineage-specific polycomb targets and de novo DNA methylation define restriction and potential of neuronal progenitors. *Mol. Cell* **30**, 755–766 (2008).
30. Nakashima, K. et al. Synergistic signaling in fetal brain by STAT3-Smad1 complex bridged by p300. *Science* **284**, 479–482 (1999).
31. Wang, J. et al. CBP histone acetyltransferase activity regulates embryonic neural differentiation in the normal and Rubinstein-Taybi syndrome brain. *Dev. Cell* **18**, 114–125 (2010).
32. Lim, D. A. et al. Chromatin remodelling factor Mll1 is essential for neurogenesis from postnatal neural stem cells. *Nature* **458**, 529–533 (2009).
33. Roopra, A., Qazi, R., Schoenike, B., Daley, T. J. & Morrison, J. F. Localized domains of G9a-mediated histone methylation are required for silencing of neuronal genes. *Mol. Cell* **14**, 727–738 (2004).
34. Boyer, L. A. et al. Polycomb complexes repress developmental regulators in murine embryonic stem cells. *Nature* **441**, 349–353 (2006).
35. Bernstein, B. E. et al. A bivalent chromatin structure marks key developmental genes in embryonic stem cells. *Cell* **125**, 315–326 (2006).
36. Creyghton, M. P. et al. Histone H3K27ac separates active from poised enhancers and predicts developmental state. *Proc. Natl. Acad. Sci. USA* **107**, 21931–21936 (2010).
37. Wang, Z. et al. Combinatorial patterns of histone acetylations and methylations in the human genome. *Nat. Genet.* **40**, 897–903 (2008).
38. Zhou, R., Niwa, S., Homma, N., Takei, Y. & Hirokawa, N. KIF26A is an unconventional kinesin and regulates GDNF-Ret signaling in enteric neuronal development. *Cell* **139**, 802–813 (2009).
39. Ju, Y. T. et al. gas7: A gene expressed preferentially in growth-arrested fibroblasts and terminally differentiated Purkinje neurons affects neurite formation. *Proc. Natl. Acad. Sci. USA* **95**, 11423–11428 (1998).
40. Williams, B. P. et al. A PDGF-regulated immediate early gene response initiates neuronal differentiation in ventricular zone progenitor cells. *Neuron* **18**, 553–562 (1997).
41. Li, S. et al. The transcription factors Egr2 and Egr3 are essential for the control of inflammation and antigen-induced proliferation of B and T cells. *Immunity* **37**, 685–696 (2012).
42. Alarcón, C. R. et al. HNRNPA2B1 is a mediator of m(6)A-dependent nuclear RNA processing events. *Cell* **162**, 1299–1308 (2015).
43. Xiao, W. et al. Nuclear m(6)A reader YTHDC1 regulates mRNA splicing. *Mol. Cell* **61**, 507–519 (2016).
44. Ben-Haim, M. S., Moshitch-Moshkovitz, S. & Rechavi, G. FTO: linking m6A demethylation to adipogenesis. *Cell Res.* **25**, 3–4 (2015).
45. Meyer, K. D. et al. 5′ UTR m(6)A promotes cap-independent translation. *Cell* **163**, 999–1010 (2015).
46. Wang, X. et al. N(6)-methyladenosine modulates messenger RNA translation efficiency. *Cell* **161**, 1388–1399 (2015).
47. Greer, E. L. & Shi, Y. Histone methylation: a dynamic mark in health, disease and inheritance. *Nat. Rev. Genet.* **13**, 343–357 (2012).
48. Karatas, H. et al. High-affinity, small-molecule peptidomimetic inhibitors of MLL1/WDR5 protein-protein interaction. *J. Am. Chem. Soc.* **135**, 669–682 (2013).

Acknowledgements

We thank L. Wang and V. Ylis from the Sanford-Burnham-Prebys Medical Discovery Institute (SBP) Animal Resources Facility for blastocyst injection and mouse maintenance; G. Garcia from the SBP Histopathology core for preparing coronal sections from frozen and paraffin-embedded mouse brains; the SBP Cell Imaging core for confocal microscopy; the SBP flow cytometry core for apoptosis analysis; B. James from the Genomics DNA Analysis Facility at SBP for high-throughput sequencing analysis; and A. Bang for critical reading of the manuscript. This work is supported by a CIHR Operating grant (No. 115194) and an NSERC Discovery Grant (327612) to Z.Z., an NCI grant (CA159859) and a CIRM (California Institute for Regenerative Medicine) Leadership Award (LA1-01747) to R.W.R., an NIGMS grant (GM062848) to G.D., NIH R01 awards (MH109978 and HG008155), an NIH RF1 award (AG054012), and an NIH U01 award (HG007610) to M.K., a CIRM Training Grant (TG2-01162) to Y.W., an NIH R01 award (R01 GM110090) and an SBP Cancer Center Pilot grant (5P30 CA030199) to J.C.Z.

Author contributions

J.C.Z. and Y.W. formulated the idea. Y.W. designed, performed and analyzed most of the experiments. Y.L. performed bioinformatics analysis under the supervision of M.K. Z.Z. provided additional suggestions relevant to bioinformatics analysis. M.Y. and Y.O. generated floxed *Mettl14* mESCs for blastocyst injection. J.W. and R.W.R. provided technical help on mouse brain sectioning and NSC culture, and helped with data analysis. S.K. and G.D. helped with dissection of early embryos. J.C.Z. and Y.W. analyzed data and wrote the paper.

Competing interests

The authors declare no competing financial interests.

Additional information

Supplementary information is available for this paper at https://doi.org/10.1038/s41593-017-0057-1.

Reprints and permissions information is available at www.nature.com/reprints.

Correspondence and requests for materials should be addressed to J.C.Z.

Publisher's note: Springer Nature remains neutral with regard to jurisdictional claims in published maps and institutional affiliations

Methods

***Mettl14* gene targeting.** *Mettl14* gene targeting vector was created by *E. coli* bacterial recombination as described[49]. NotI-ApaI fragment including intron 1 to 5 of *Mettl14* in the fosmid WI1-205L1 (CHORI) was cloned into pGEM11-DTA2L vector[50], yielding pGEM-Mettl14(1-5)-DTA. Two primer pairs (M14-L50F and M14-L50R, the left arm for bacterial recombination; LoxP-LF and LoxP-LR) were annealed and cloned into XhoI/HindIII of pBS-2xFRT-Zeo, derivative of pBS-2xF5-Zeo[51]. The PCR fragment including *Mettl14* intron 1 to 2 with *loxP* site (primer pair, M14-ex2F and M14-ex2R-LoxP) digested by BstBI-MluI and right arm adaptor (annealed primer pair, Mettl14-R50F and Mettl14-R50R) were cloned into the vector with the left arm. The splice acceptor (SA)-internal ribosomal entry site (Ires)-hygromycin resistance gene (Hyg)-tandem polyadenylation signals (tpA) cassette of pGEM-SA-Ires-Hyg-tpA was cloned into NheI-PmlI of the vector with left and right arms[51]. The bacterial targeting vector was digested by AgeI- NotI to remove vector backbone and was transfected into *E. coli* strain SW106 containing pGEM-Mettl14(1-5)-DTA for bacterial recombination, yielding Mettl14 targeting vector for mouse ES cells.

Mettl14 ES targeting vector was linearized by NotI and transfected into G4 male ES cells as described[52,53]. 24 h after transfection, 150 μg/ml Hygromycin was added to the ES medium. Hygromycin-resistant ES colonies were picked 10 d after transfection. Targeting of Mettl14 was confirmed by genomic PCR analysis using primer pairs: M14cF and SA-R for 5′-end; UptpA-F and M14-cR for 3′-end.

Generation of Mettl14 conventional and conditional knockout mice. Positive ES clones were used for injection into c57 blastocysts and generation of chimerical mice. To produce *Mettl14*$^{f/+}$ mice, the chimeras were crossed with wild-type c57 for germ line transmission and then crossed with *Atcb-Flpe* transgenic mice (The Jackson Laboratory, # 003800) to remove FRT flanked selection cassette. Male *Mettl14*$^{f/+}$ mice were crossed to female *EIIa-Cre* transgenic mice (The Jackson Laboratory, # 003724) to obtain *Mettl14*$^{+/-}$ mice, and *Mettl14*$^{+/-}$ mice were intercrossed to obtain *Mettl14*–conventional knockout mice. Sex of embryos was determined.

To conditionally knock out *Mettl14* in brain, floxed Mettl14 mice were bred with *Nestin-Cre* transgenic mice (The Jackson Laboratory, # 003771) to generate *Mettl14*$^{f/f}$*;Nestin-cre*. Sex of embryos was not determined. Mice were maintained at the Sanford Burnham Prebys Medical Discovery Institute Institutional animal facility, and experiments were performed in accordance with experimental protocols approved by local Institutional Animal Care and Use Committees.

Genotyping. Genotyping was performed using the MyTaq Extract-PCR kit (Bioline) with primer sets corresponding to the primer list table (Supplementary Table 7).

Injection of S-phase tracer. IdU/BrdU double-labeling was performed as previously described[18]. Briefly, pregnant females were injected intraperitoneally with Iododeoxyuridine (IdU, Sigma) (100 mg/kg body weight) and 1.5 h later with the same dose of BrdU (Sigma) and killed after 0.5 h.

For BrdU single-labeling, pregnant females were injected intraperitoneally with BrdU (100 mg/kg body weight) and killed after 0.5 or 24 h.

Immunohistochemistry. Frozen sections were boiled in citrate buffer, pH 6.0 (Sigma), penetrated in 0.25% Triton X-100 in PBS for 30 min at room temperature and blocked in PBST (PBS with 0.2% Tween-20) containing 10% normal goat serum (Abcam). Sections were incubated with primary antibody at 4 °C overnight. Secondary antibodies were applied to sections for 2 h at room temperature. The primary antibodies used were as follows: rabbit anti-Mettl14 (1:500; Sigma, Cat. # HPA038002; immunohistochemistry validation and peer-reviewed citations at https://www.sigmaaldrich.com/catalog/product/sigma/hpa038002?lang=en&region=US), Rabbit anti-Satb2 (1:500, Abcam, Cat. # Ab92446; immunohistochemistry validation and peer-reviewed citations at http://www.abcam.com/satb2-antibody-epncir130a-ab92446.html), Rabbit anti-Tbr1 (1:200, Abcam, Cat. # Ab31940; immunohistochemistry validation and peer-reviewed citations at http://www.abcam.com/tbr1-antibody-ab31940.html), rabbit anti-Sox5 (1:200; Abcam, Cat. # Ab94396; immunohistochemistry validation and peer-reviewed citations at http://www.abcam.com/sox5-antibody-chip-grade-ab94396.html), rabbit anti-Cux1 (1:100; Santa Cruz, Cat. # sc-13024; immunohistochemistry validation and peer-reviewed citations at https://www.scbt.com/scbt/product/cdp-antibody-m-222), rabbit anti-Pax6 (1:300; Biolegend, Cat. # PRB-278P; immunohistochemistry validation and peer-reviewed citations at https://www.biolegend.com/en-us/products/purified-anti-pax-6-antibody-11511), rat anti-BrdU (1:200; Abcam, Cat. # Ab6326; immunohistochemistry validation and peer-reviewed citations at http://www.abcam.com/brdu-antibody-bu175-icr1-ab6326.html), mouse anti-IdU/BrdU (1:50; BD bioscience, Cat. # 347580; immunohistochemistry validation and peer-reviewed citations at https://www.bioz.com/result/mouse%20anti%20brdu/product/BD%20Biosciences/?r=4.31&cf=0&uq=BrdU%20clone%20B44), rabbit anti-Ki67 (1:400, Cell Signaling, Cat. # 12202; immunohistochemistry validation and peer-reviewed citations at https://www.cellsignal.com/products/primary-antibodies/ki-67-d3b5-rabbit-mab-mouse-preferred-ihc-formulated/12202), rat anti-phospho histone 3 (1:300; Abcam, Cat. # Ab10543; immunohistochemistry validation and peer-reviewed citations at http://www.abcam.com/histone-h3-phospho-s28-antibody-hta28-ab10543.html), rabbit anti-Cleaved Caspase-3 (1:600; Cell Signaling, Cat. # 9661; immunohistochemistry validation and peer-reviewed citations at https://www.cellsignal.com/products/primary-antibodies/cleaved-caspase-3-asp175-antibody/9661), rabbit anti-NeuroD2 (1:1,000; Abcam, Cat. # Ab104430; immunohistochemistry validation and peer-reviewed citations at http://www.abcam.com/neurod2-antibody-ab104430.html), rabbit anti-Tbr2 (1:500, Abcam, Cat. # Ab23345; immunohistochemistry validation and peer-reviewed citations at http://www.abcam.com/tbr2-eomes-antibody-chip-grade-ab23345.html), mouse anti-Tuj1 (1:1,000; Stemcell Tech., Cat. # 01409; immunohistochemistry validation at https://www.stemcell.com/anti-beta-tubulin-iii-antibody-clone-tuj1.html and peer-reviewed citations at https://www.bioz.com/result/tuj1/product/STEMCELL%20Technologies%20Inc/?r=3.00&cf=0&uq=Stemcell%20Tech%20tuj1). Secondary antibodies were Alexa Fluor 488 Goat anti-Rabbit IgG (Thermo Fisher Scientific, Cat. # A-11008; 1:1,000; immunohistochemistry validation and peer-reviewed citations at https://www.thermofisher.com/antibody/product/Goat-anti-Rabbit-IgG-H-L-Cross-Adsorbed-Secondary-Antibody-Polyclonal/A-11008), Alexa Fluor 488 Goat anti-Mouse IgG (Thermo Fisher Scientific, Cat. # A-11001; 1:1,000; immunohistochemistry validation and peer-reviewed citations at https://www.thermofisher.com/antibody/product/Goat-anti-Mouse-IgG-H-L-Cross-Adsorbed-Secondary-Antibody-Polyclonal/A-11001), Texas Red-X Goat anti-Rat IgG (Thermo Fisher Scientific, Cat. # T-6392; 1:1,000; immunohistochemistry validation and peer-reviewed citations at https://www.thermofisher.com/antibody/product/Goat-anti-Rat-IgG-H-L-Cross-Adsorbed-Secondary-Antibody-Polyclonal/T-6392). DAPI (Thermo Fisher Scientific, Cat. # 62248; 1:1,000) was used as nuclear counterstaining and slides were mounted in FluroSave reagent (Millipore, Cat. # 345789).

For BrdU staining, sections were treated with 2 N HCl at 37 °C for 30 min and 0.1 M borate buffer, pH 8.5, for 10 min at room temperature.

Pax6-Tbr2 and Pax6-Mettl14 co-staining were performed according to the protocol described in a previous paper[54]. In brief, sections were incubated with highly diluted (1:30,000) primary antibody overnight at 4 °C and biotinylated goat anti-rabbit secondary antibody for 1 h at room temperature. The signal was amplified with the horseradish-peroxidase-based Vectastain ABC Kit (Vector Laboratories, Cat. # PK-6101) and Cyanine 3 Tyramide System (Perkin Elmer, Cat. # NEL704A001KT).

Fluorescence images were acquired by Zeiss LSM 710 confocal microscope and analyzed in ImageJ software.

NPC isolation and culture. Cortex region was dissected out from embryonic brains and triturated by pipetting. Dissociated cells were cultured as neurospheres with NeuroCult Proleferation Medium (Stemcell Tech.) according to the manufacturer's protocols. Lentiviral constructs harboring shRNAs against Alkbh5 or Fto were purchased from Sigma-Aldrich (see below for details). Stable knockdown lines were generated using standard viral infection and puromycin selection (2 μg/ml).

shRNA RNA sequences. shAlkbh5-1: 5′-CCTATGAGTCCTCGGAAGATT-3′
shAlkbh5-1: 5′-GATCCTGGAAATGGACAAAGA-3′
shFto-1: 5′-GTCTCGTTGAAATCCTTTGAT-3′
shFto-1: 5′-TAGTCTGACTTGGTGTTAAAT-3′

Purification of mRNA. Total RNA was isolated using TRIZOL (Invitrogen) and treated with DNase I (Roche). Polyadenylated mRNA was purified using the GenElute mRNA Miniprep Kit (Sigma-Aldrich), and residual ribosomal RNA was depleted with RiboMinus Eukaryote System v2 (Life Technologies).

2D-TLC. 2D-TLC was performed similarly as described[55]. Briefly, 500 ng purified polyA+/ribo– RNA was digested with 20 U RNase T1 (Thermo Fisher Scientific) in 20 μl 1× PNK buffer for 2 h at 37 °C. The digested RNA was labeled using 10 U T4 PNK (Thermo Fisher Scientific) and 1 μl γ-^{32}P-ATP (6,000 Ci/mmol, 150 mCi/ml, Perkin-Elmer) and for 1 h at 37 °C and precipitated. The RNA pellet was resuspended in 5 μl buffer containing 25 mM NaCl, 2.5 mM $ZnSO_4$ and 1 U nuclease P1 (Sigma) and incubated at 37 °C overnight. 1 μl product was loaded onto a PEI-Cellulose TLC plate (Millipore) and developed in isobutyric acid: 0.5 M NH_4OH (5:3, v/v) as first dimension and isopropanol:HCl:water (70:15:15, v/v/v) as second dimension. After development, the plate was exposed to a phosphor screen and scanned using a FujiFilm FLA-5100 imager.

m^{6}A dot-blot. Purified polyA+ RNA was blotted to a nylon membrane (Millipore) using Bio-Dot Microfiltration Apparatus (Bio-Rad). After cross-linking with a UV cross-linker (Spectroline), the membrane was blocked with nonfat milk in TBST and then incubated with antibody to m^{6}A (Synaptic Systems, Cat. # 202 003, 1:1,000; dot blot validation and peer-reviewed citations at https://www.sysy.com/products/m6a/facts-202003.php) then an HRP-conjugated antibody to rabbit IgG (SouthernBiotech, Cat # 4030-05, 1:5,000; immunoblotting validation and peer-reviewed citations at https://www.southernbiotech.com/?catno=4030-05&type=Polyclonal#&panel1-1). After incubation with the Immobilon Western Chemiluminescent HRP Substrate (Millipore), the membrane was exposed to autoradiography film (Kodak).

Neurosphere formation assay. Dissociated NPCs were seeded into a 96-well plate at 400 cells per well and cultured for 7 d, then the 96-well plate was scanned using a Celigo Imaging Cytometer (Nexcelom Bioscience) and the number and size of neurospheres were measured.

Immunostaing of cultured NPCs and TUNEL assay. NPCs cultured for 7 d in vitro were dissociated and plated into chamber slides. The slides were stained with antibody to Tuj1 (1:1,000; Stemcell Tech., Cat. # 01409). TUNEL assay was performed using the Click-iT Plus kit (Thermo Fisher Scientific) according to the manufacturer's protocols.

Apoptosis FACS. Dissociated NPCs were incubated with the Dead Cell Apoptosis Kit with Annexin V Alexa Fluor 488 and propidium iodide (Thermo Fisher Scientific) according to the manufacturer's protocols and analyzed by LSRFortessa Cell Analyzer (BD Biosciences).

MTT assay. Dissociated NPCs were seeded into a 96-well plate. Cell numbers were measured using the Cell Growth Determination Kit (Sigma) according to the manufacturer's protocols at different time points.

Western blot analysis. Proteins were separated on SDS-PAGE gel, blotted onto PVDF membrane and detected with primary antibodies to Gapdh (Cell Signaling, Cat. # 5174, 1:20,000; western blot validation and peer-reviewed citations at https://www.cellsignal.com/products/primary-antibodies/gapdh-d16h11-xp-rabbit-mab/5174), Mettl14 (Sigma-Aldrich, Cat. # HPA038002, 1:5,000; western blot validation and peer-reviewed citations at https://www.sigmaaldrich.com/catalog/product/sigma/hpa038002?lang=en&region=US), Flag (Sigma-Aldrich, Cat. # 1804, 1:10,000; western blot validation and peer-reviewed citations at https://www.sigmaaldrich.com/catalog/product/sigma/f1804?lang=en&region=US), Alkhb5 (Sigma-Aldrich, Cat. # HPA007196, 1:2,000; western blot validation and peer-reviewed citations at https://www.sigmaaldrich.com/catalog/product/sigma/hpa007196?lang=en&region=US) and Fto (PhosphoSolutions, Cat. # 597-FTO, 1:1,000; western blot validation and peer-reviewed citations at https://www.phosphosolutions.com/shop/fto-antibody/). Secondary antibodies were Goat Anti-Rabbit IgG-HRP (SouthernBiotech, Cat. # 4030-05; 1:10,000; western blot validation and peer-reviewed citations at https://www.southernbiotech.com/?catno=4030-05&type=Polyclonal#&panel1-1) and Rabbit Anti-Mouse IgG-HRP (SouthernBiotech, Cat. # 6170-05; 1:10,000; western blot validation and peer-reviewed citations at https://www.southernbiotech.com/?catno=6170-05&type=Polyclonal).

Histone extraction and quantitative western blot analysis. Histones were extracted from NPCs cultured for 7 d in vitro using a Histone Extraction Kit (Abcam) according to the manufacturer's protocols. Histone lysates were separated on SDS-PAGE gel, blotted onto Immobilon-FL PVDF membrane (Millipore, Cat. # IPFL00010) and incubated with primary antibodies including rat anti-H3 (Active Motif, Cat. # 61647; 1:2000; western blot validation and peer-reviewed citations at https://www.activemotif.com/catalog/details/61647/histone-h3-antibody-mab-clone-1c8b2), rabbit anti-H3K4me1 (Abcam, Cat. # Ab8895; 1:4,000; western blot validation and peer-reviewed citations at http://www.abcam.com/histone-h3-mono-methyl-k4-antibody-chip-grade-ab8895.html), rabbit anti-H3K4me3 (Abcam, Cat. # Ab8580; 1:2,000; western blot validation and peer-reviewed citations at http://www.abcam.com/histone-h3-tri-methyl-k4-antibody-chip-grade-ab8580.html), rabbit anti-H3K9me3 (Abcam, Cat. # Ab8898; 1:2,000; western blot validation and peer-reviewed citations at http://www.abcam.com/histone-h3-tri-methyl-k9-antibody-chip-grade-ab8898.html), rabbit anti-H3K27me3 (Millipore, Cat. # 07-449; 1:2,000; western blot validation at http://www.emdmillipore.com/US/en/product/Anti-trimethyl-Histone-H3-Lys27-Antibody,MM_NF-07-449 and peer-reviewed citations at https://www.bioz.com/result/antih3k27me3/product/Millipore/?r=4.88&cf=0&uq=Millipore, Cat. - 07%252D449), rabbit anti-H3K9ac (Active Motif, Cat. # 39917; 1:2,000; western blot validation at http://www.activemotif.com/catalog/details/39917 and peer-reviewed citations at https://www.bioz.com/result/h3k9ac/product/Active%20Motif/?r=4.14&cf=0&uq=Active%20Motif, Cat. - 39917), rabbit anti-H3K27ac (Abcam, Cat. # Ab4729; 1:2000; western blot validation and peer-reviewed citations at http://www.abcam.com/histone-h3-acetyl-k27-antibody-chip-grade-ab4729.html), and rabbit anti-H3ac (Active Motif, Cat. # 39139; 1:2,000; western blot validation at http://www.activemotif.com/catalog/details/39139/histone-h3ac-pan-acetyl-antibody-pab-1 and peer-reviewed citations at https://www.bioz.com/result/chip%20validated%20antibodies%20h3%20pan%20acetyl/product/Active%20Motif/?r=3.00&cf=0&uq=Active%20Motif, Cat. - 39139), rabbit anti-H2AK119Ubi (Cell Signaling, Cat. # 8240; 1:4000; western blot validation and peer-reviewed citations at https://www.cellsignal.com/products/primary-antibodies/ubiquityl-histone-h2a-lys119-d27c4-xp-rabbit-mab/8240), mouse anti-H2BK120Ubi (Active Motif, Cat. # 39623; 1:2000; western blot validation at http://www.activemotif.com/catalog/details/39623/histone-h2b-ubiquityl-lys120-antibody-mab-clone-56 and peer-reviewed citations at https://www.bioz.com/result/h2bub1/product/Active%20Motif/?r=3.00&cf=0&uq=Active%20Motif Cat. - 39623), rabbit anti-H3S28pho (Abcam, Cat. # Ab10543; 1:2000; western blot validation at http://www.abcam.com/histone-h3-phospho-s28-antibody-hta28-ab10543.html and peer-reviewed citations at https://www.bioz.com/result/ab10543/product/Abcam/?r=3.00&cf=0&uq=Abcam, Cat. - Ab10543). Secondary antibodies were IRDye 800CW Goat anti-Rat IgG (LI-COR Biosciences, Cat. # 925-32219; 1:20,000; western blot validation and peer-reviewed citations at https://www.bioz.com/result/irdye%20800%20goat%20anti%20rat%20igg/product/LI-COR/?r=3.42&cf=0&uq=IRDye%20800%20Goat%20anti-Rat%20IgG), IRDye 680RD Goat anti-Rabbit IgG (LI-COR Biosciences, Cat. # 925-68071; 1:20,000; western blot validation and peer-reviewed citations at https://www.bioz.com/result/irdye%20680rd%20conjugated%20goat%20anti%20rabbit%20igg%20secondary%20antibody/product/LI-COR/?r=3.53&cf=0&uq=IRDye%20680RD%20Goat%20anti-Rabbit%20IgG), IRDye 680RD Goat anti-Mouse IgG (LI-COR Biosciences, Cat. # 925-68070; 1:20,000; western blot validation and peer-reviewed citations at https://www.bioz.com/result/irdye%20680rd%20goat%20anti%20mouse%20igg/product/LI-COR/?r=4.95&cf=0&uq=IRDye%20680RD%20Goat%20anti-Mouse%20IgG). Membranes were scanned by Odyssey Imager (LI-COR Biosciences) and quantified using Image Studio Lite (LI-COR Biosciences).

RT-qPCR. DNase-I-treated total RNA was used to synthesize cDNA using an iScript cDNA synthesis kit (Bio-Rad) according to the manufacturer's protocols. qPCR was performed with primer sets corresponding to the primer list table (Supplementary Table 7) and using iTaq Universal SYBR Green Supermix (Bio-Rad) on a BioRad CFX96 Touch Real-Time PCR Detection.

RNA-seq analysis. *RNA-seq alignment.* Tuxedo-suite was used for the entire RNA-seq analyses[56]. Specifically, TopHat2 (v2.1.0) was used to align RNA-seq reads to the mouse genome (mm10). To ensure correct alignment especially for assigning the spliced reads to the correct transcripts, we supplied the software with an existing transcript reference annotation from RefSeq with option–GTF. The RefSeq annotation is available as the iGenome project at the TopHat website (https://ccb.jhu.edu/software/tophat/igenomes.shtml). Other settings of the aligner were left to the default.

Transcript assembly. We then supplied the alignment BAM files from TopHat2 to Cufflinks to perform transcript assembly and expression estimation. The assembly was guided by the above RefSeq annotations with option–GTF-guide. We also turn on the multi-read correction (--multi-read-correct) and fragment bias correction options (--frag-bias-correct $genome) to correct for the sequencing biases. Other settings of the assembler were left to the default.

Differential analysis. We assembled transcripts in each sample library and biological replicate separately. In the end, we ran Cuffmerge to combine all assembled transcripts into a merged custom annotation file (merged.gtf) for the differential expression analysis. In particular, we ran Cuffdiff to compare between M14 knockout mutant and wild-type libraries using the read alignment files from TopHat2 as input and the above custom annotation file as reference. The 3 biological replicates per condition were used to estimate the dispersion in the negative binomial likelihood function modeled by Cuffdiff. We also enabled --multi-read-correct and --frag-bias-correct to improve estimation. The main output from Cuffdiff that were used for downstream analysis in this paper were the "gene_exp.diff" and "genes.read_group_tracking" (default output names from the software), which provide the differential expression statistical results and the actual expression estimate in terms of FPKM, respectively. Significant fold-change was determined based on FDR < 0.05 (as the default threshold of the Cuffdiff program).

GO analysis. GO analyses were performed by DAVID. Differentially expressed genes had an adjusted $P < 0.01$ and a twofold or greater expression difference.

ChIP-seq analysis. *Chromatin immunoprecipitation (ChIP).* For ChIP experiments, NPCs cultured for 7 d in vitro were harvested and cross-linked for 5 min at room temperature using 1% formaldehyde. Cells were lysed by rotation for 10 min at 4 °C in cell lysis buffer (20 mM Tris, pH 8, 85 mM KCl, 0.5% NP-40, protease inhibitor cocktail). Nuclei were pelleted and re-suspended in nuclei lysis buffer (50 mM Tris, pH 8, 10 mM EDTA, 0.25% SDS, protease inhibitor cocktail). Chromatin was sheared by Covaris S2 using AFA microtube and a low cell chromatin shearing protocol for 12 min. Lysates were cleared by centrifugation at 20,000*g* at 4 °C for 5 min and used as IP inputs. IP was done using the MAGnify Chromatin Immunoprecipitation System (Thermo Fisher Scientific) according to the manufacturer's protocols. The antibodies used were as follows: rabbit anti-H3K27ac (Abcam, Cat. # Ab4729, Lot. # GR312658-1; ChIP validation and peer-reviewed citations at http://www.abcam.com/histone-h3-acetyl-k27-antibody-chip-grade-ab4729.html), rabbit anti-H3K27me3 (Millipore, Cat. # 07-449, Lot. # 2686928; ChIP validation at http://www.emdmillipore.com/US/en/product/Anti-trimethyl-Histone-H3-Lys27-Antibody,MM_NF-07-449 and peer-reviewed citations at https://www.bioz.com/result/antih3k27me3/product/Millipore/?r=4.88&cf=0&uq=Millipore, Cat. - 07%252D449). Chromatin samples were sent for high-throughput sequencing.

ChIP-seq alignment, peak calling, and comparison. To align ChIP-seq DNA reads to the reference mm10 genome, we used Bowtie2 (v2.3.1)[57] with the default options

except that "--broad" was turned on for calling broad peaks. Each ChIP library in each biological replicate was compared against the DNA input background library in the corresponding cell type + condition. Specifically, histone marks H3K4me3 and H3K27ac in wild-type and M14 KO mutant of mouse neural progenitor cell (NPC) were compared with the DNA input in wild-type and M14 KO NPC, respectively. Default cutoffs of FDR < 0.05 were used to determine ChIP-seq peaks relative to the input libraries. The main outputs from MACS2 were the broadPeak files in BED format, which we used for downstream comparison among the experimental conditions and with other cognate genome-wide results (that is, RNA-seq and RIP-seq).

meRIP-seq analysis. *meRIP.* meRIP was performed as previously described[4]. Briefly, total RNA was extracted using Trizol reagent (Invitrogen). RNA was treated with RNase-free DNase I (Roche) to deplete DNA contamination. PolyA RNA was purified using a GenElute mRNA Miniprep Kit (Sigma-Aldrich) as per the manufacturer's instructions and fragmented using an RNA fragmentation kit (Ambion). 200 µg of fragmented RNA was incubated with 3 µg anti-m6A (Synaptic Systems, catalog number 202 003; RIP validation and peer-reviewed citations at https://www.sysy.com/products/m6a/facts-202003.php) in RIP buffer (150 mM NaCl, 10 mM Tris and 0.1% NP-40) for 2 h at 4 °C, followed by the addition of washed protein A/G magnetic beads (Millipore) and incubation at 4 °C for a further 2 h. Beads were washed 6 times in RIP buffer and incubated with 50 µl immunoprecipitation buffer containing 0.5 mg ml^{-1} m^{6}AMP (Sigma-Aldrich) to elute RNA. Immunoprecipitated RNA was extracted with phenol/chloroform, and RNA samples were sent for high-throughput sequencing.

meRIP-seq alignment and peak calling. We used Tophat2 to align reads to the mouse reference mm10 genome with default setting and RefSeq annotations as a guide (that is, the same method as in the RNA-seq analysis). To call RIP-seq peaks, we used MACS2 with default settings except for enabling the --broad option (that is, the same as in the ChIP-seq analysis).

RNA stability assay. Actinomycin D (Sigma-Aldrich) at 5 µg/ml was added to NPC culture. After 0, 3 or 6 h of incubation, cells were collected and RNAs were isolated for qPCR.

Statistical analysis. All data are expressed as mean ± s.d., as indicated in the figure legends. Statistical analyses were completed with Prism GraphPad 7. Data comparing WT versus *Mettl14* Het and KO phenotypes and data of inhibitor treatment were analyzed using one-way ANOVA followed by Bonferroni's multiple comparisons test. Data comparing WT versus *Mettl14*-KO were analyzed using unpaired *t*-test. NSC growth curves were analyzed using two-way ANOVA followed by Bonferroni's multiple comparisons test. RNA stability data comparing WT versus *Mettl14*-KO NSCs were analyzed using two-way ANOVA.

The association between m^{6}A targets and differential gene expression in *Mettl14*-KO versus nondeleted control NSCs were determined by Fisher's exact test. Correlation analyses between changes in ChIP peak intensity and changes in gene expression were done using Pearson correlation analysis. No statistical methods were used to pre-determine sample sizes but our sample sizes are similar to those reported in previous publications[1,2,4,13,16,18]. Data distribution was assumed to be normal but this was not formally tested. There was no randomization in the organization of the experimental conditions. Data collection and analysis were not performed blind to the conditions of the experiments. We did not exclude any animals for data point from the analysis.

Accession codes. The data discussed in this publication have been deposited in NCBI's Gene Expression Omnibus and are accessible through GEO Series accession number GSE104686.

Life Sciences Reporting Summary. Further information on experimental design is available in the Life Sciences Reporting Summary.

Data availability. RNA-seq and ChIP-seq data are accessible at NCBI GEO: GSE104686. The remaining data that support the findings of this study are available from the corresponding author upon reasonable request.

References

49. Lee, E. C. et al. A highly efficient *Escherichia coli*-based chromosome engineering system adapted for recombinogenic targeting and subcloning of BAC DNA. *Genomics* **73**, 56–65 (2001).
50. Ogawa, Y. & Lee, J. T. Xite, X-inactivation intergenic transcription elements that regulate the probability of choice. *Mol. Cell* **11**, 731–743 (2003).
51. Yamada, N. et al. Xist exon 7 contributes to the stable localization of Xist RNA on the inactive X-chromosome. *PLoS Genet.* **11**, e1005430 (2015).
52. Daikoku, T. et al. Lactoferrin-iCre: a new mouse line to study uterine epithelial gene function. *Endocrinology* **155**, 2718–2724 (2014).
53. George, S. H. et al. Developmental and adult phenotyping directly from mutant embryonic stem cells. *Proc. Natl. Acad. Sci. USA* **104**, 4455–4460 (2007).
54. Arai, Y. et al. Neural stem and progenitor cells shorten S-phase on commitment to neuron production. *Nat. Commun.* **2**, 154 (2011).
55. Bodi, Z., Button, J. D., Grierson, D. & Fray, R. G. Yeast targets for mRNA methylation. *Nucleic Acids Res.* **38**, 5327–5335 (2010).
56. Trapnell, C. et al. Differential gene and transcript expression analysis of RNA-seq experiments with TopHat and Cufflinks. *Nat. Protoc.* **7**, 562–578 (2012).
57. Langmead, B. & Salzberg, S. L. Fast gapped-read alignment with Bowtie 2. *Nat. Methods* **9**, 357–359 (2012).

nature research

Corresponding author(s): Jing Crystal Zhao

☐ Initial submission ☐ Revised version ☒ Final submission

Life Sciences Reporting Summary

Nature Research wishes to improve the reproducibility of the work that we publish. This form is intended for publication with all accepted life science papers and provides structure for consistency and transparency in reporting. Every life science submission will use this form; some list items might not apply to an individual manuscript, but all fields must be completed for clarity.

For further information on the points included in this form, see Reporting Life Sciences Research. For further information on Nature Research policies, including our data availability policy, see Authors & Referees and the Editorial Policy Checklist.

Experimental design

1. Sample size

Describe how sample size was determined.

No statistical methods were used to determine sample size. We chose the sample size based on literatures in the field.

2. Data exclusions

Describe any data exclusions.

No exclusions

3. Replication

Describe whether the experimental findings were reliably reproduced.

Phenotypes observed are robust and were reliably reproduced. All experiments on mice embryos and newborns were repeated using at least 3 independent litters that consist all reported genotypes.

4. Randomization

Describe how samples/organisms/participants were allocated into experimental groups.

Mice were allocated to different groups based on the genotypes. No randomization was used in this study.

5. Blinding

Describe whether the investigators were blinded to group allocation during data collection and/or analysis.

Mice were allocated to different groups based on the genotypes. No blinding was used in this study.

Note: all studies involving animals and/or human research participants must disclose whether blinding and randomization were used.

6. Statistical parameters

For all figures and tables that use statistical methods, confirm that the following items are present in relevant figure legends (or in the Methods section if additional space is needed).

n/a	Confirmed
☐	☒ The exact sample size (*n*) for each experimental group/condition, given as a discrete number and unit of measurement (animals, litters, cultures, etc.)
☐	☒ A description of how samples were collected, noting whether measurements were taken from distinct samples or whether the same sample was measured repeatedly
☐	☒ A statement indicating how many times each experiment was replicated
☐	☒ The statistical test(s) used and whether they are one- or two-sided (note: only common tests should be described solely by name; more complex techniques should be described in the Methods section)
☐	☒ A description of any assumptions or corrections, such as an adjustment for multiple comparisons
☐	☒ The test results (e.g. *P* values) given as exact values whenever possible and with confidence intervals noted
☐	☒ A clear description of statistics including central tendency (e.g. median, mean) and variation (e.g. standard deviation, interquartile range)
☐	☒ Clearly defined error bars

See the web collection on statistics for biologists for further resources and guidance.

Software

Policy information about availability of computer code

7. Software

Describe the software used to analyze the data in this study.	Prism GraphPad 7, ImageJ, FACSDiva 6, Image Studio Lite, TopHat2, Cufflinks, Cuffmerge, Cuffdiff, Bowtie2, MACS2, DAVID

For manuscripts utilizing custom algorithms or software that are central to the paper but not yet described in the published literature, software must be made available to editors and reviewers upon request. We strongly encourage code deposition in a community repository (e.g. GitHub). *Nature Methods* guidance for providing algorithms and software for publication provides further information on this topic.

Materials and reagents

Policy information about availability of materials

8. Materials availability

Indicate whether there are restrictions on availability of unique materials or if these materials are only available for distribution by a for-profit company.	No specific restrictions.

9. Antibodies

Describe the antibodies used and how they were validated for use in the system under study (i.e. assay and species).	For Immunohistochemistry. The primary antibodies used were as follows: rabbit anti-Mettl14 (1:500; Sigma, Cat. # HPA038002; immunohistochemistry valida¬tion and peer-reviewed citations at https://www.sigmaaldrich.com/catalog/product/sigma/hpa038002?lang=en&region=US), Rabbit anti-Satb2 (1:500, Abcam, Cat. # Ab92446; immunohistochemistry valida¬tion and peer-reviewed citations at http://www.abcam.com/satb2-antibody-epncir130a-ab92446.html), Rabbit anti-Tbr1 (1:200, Abcam, Cat. # Ab31940; immunohistochemistry valida¬tion and peer-reviewed citations at http://www.abcam.com/tbr1-antibody-ab31940.html), rabbit anti-Sox5 (1:200; Abcam, Cat. # Ab94396; immunohistochemistry valida¬tion and peer-reviewed citations at http://www.abcam.com/sox5-antibody-chip-grade-ab94396.html), rabbit anti-Cux1 (1:100; Santa Cruz, Cat. # sc-13024; immunohistochemistry valida¬tion and peer-reviewed citations at https://www.scbt.com/scbt/product/cdp-antibody-m-222), rabbit anti-Pax6 (1:300; Biolegend, Cat. # PRB-278P; immunohistochemistry valida¬tion and peer-reviewed citations at https://www.biolegend.com/en-us/products/purified-anti-pax-6-antibody-11511), rat anti-BrdU (1:200; Abcam, Cat. # Ab6326; immunohistochemistry valida¬tion and peer-reviewed citations at http://www.abcam.com/brdu-antibody-bu175-icr1-ab6326.html), mouse anti-IdU/BrdU (1:50; BD bioscience, Cat. # 347580; immunohistochemistry valida¬tion and peer-reviewed citations at https://www.bioz.com/result/mouse anti brdu/product/BD Biosciences/?r=4.31&cf=0&uq=BrdU clone B44), rabbit anti-Ki67 (1:400, Cell Signaling, Cat. # 12202; immunohistochemistry valida¬tion and peer-reviewed citations at https://www.cellsignal.com/products/primary-antibodies/ki-67-d3b5-rabbit-mab-mouse-preferred-ihc-formulated/12202), rat anti-phospho histone 3 (1:300; Abcam, Cat. # Ab10543; immunohistochemistry valida¬tion and peer-reviewed citations at http://www.abcam.com/histone-h3-phospho-s28-antibody-hta28-ab10543.html), rabbit anti-Cleaved Caspase-3 (1:600; Cell Signaling, Cat. # 9661; immunohistochemistry valida¬tion and peer-reviewed citations at https://www.cellsignal.com/products/primary-antibodies/cleaved-caspase-3-asp175-antibody/9661), rabbit anti-NeuroD2 (1:1,000; Abcam, Cat. # Ab104430; immunohistochemistry valida¬tion and peer-reviewed citations at http://www.abcam.com/neurod2-antibody-ab104430.html), rabbit anti-Tbr2 (1:500, Abcam, Cat. # Ab23345; immunohistochemistry valida¬tion and peer-reviewed citations at http://www.abcam.com/tbr2-eomes-antibody-chip-grade-ab23345.html), mouse anti-Tuj1 (1:1,000; Stemcell Tech., Cat. # 01409; immunohistochemistry valida¬tion at https://www.stemcell.com/anti-beta-tubulin-iii-antibody-clone-tuj1.html and peer-reviewed citations at https://www.bioz.com/result/tuj1/product/STEMCELL Technologies Inc/?r=3.00&cf=0&uq=Stemcell Tech tuj1). Secondary antibodies were Alexa Fluor 488 Goat anti-Rabbit IgG (Thermo Fisher Scientific, Cat. # A-11008; 1:1,000; immunohistochemistry valida¬tion and peer-reviewed citations at https://www.thermofisher.com/antibody/product/Goat-anti-Rabbit-IgG-H-L-Cross-Adsorbed-Secondary-Antibody-Polyclonal/A-11008), Alexa Fluor 488 Goat anti-Mouse IgG (Thermo Fisher Scientific, Cat. # A-11001; 1:1,000; immunohistochemistry valida-tion and peer-reviewed citations at https://www.thermofisher.com/antibody/product/Goat-anti-Mouse-IgG-H-L-Cross-Adsorbed-Secondary-Antibody-Polyclonal/A-11001), Texas Red-X Goat anti-Rat IgG (Thermo Fisher Scientific, Cat. # T-6392; 1:1,000; immunohistochemistry valida¬tion and peer-reviewed citations at https://www.thermofisher.com/antibody/product/Goat-anti-Rat-IgG-H-L-Cross-Adsorbed-Secondary-Antibody-

10. Eukaryotic cell lines

a. State the source of each eukaryotic cell line used.

The only cell lines used in the study are primary cultured E14.5/E17.5/P0 mouse NSCs.

b. Describe the method of cell line authentication used.

NSC genotypes were determined by genomic PCR.

c. Report whether the cell lines were tested for mycoplasma contamination.

All NSC lines were tested negative for mycoplasma contamination.

d. If any of the cell lines used are listed in the database of commonly misidentified cell lines maintained by ICLAC, provide a scientific rationale for their use.

No commonly misidentified cell lines were used in this study.

Animals and human research participants

Policy information about studies involving animals; when reporting animal research, follow the ARRIVE guidelines

11. Description of research animals

Provide details on animals and/or animal-derived materials used in the study.

Genetically modified c57 mice were used in this study. Both male and female embryos (E7.5, E8.5, E9.5, E13.5, E15.5, E17.5) or neonatal mice (P0 - P7) were used for analysis.

Policy information about studies involving human research participants

12. Description of human research participants

Describe the covariate-relevant population characteristics of the human research participants.

This study did not involve human research participants.

nature research

Corresponding author(s): Jing Crystal Zhao

☐ Initial submission ☐ Revised version ☒ Final submission

ChIP-seq Reporting Summary

Form fields will expand as needed. Please do not leave fields blank.

Data deposition

1. For all ChIP-seq data:

☒ a. Confirm that both raw and final processed data have been deposited in a public database such as GEO.

☒ b. Confirm that you have deposited or provided access to graph files (e.g. BED files) for the called peaks.

2. Provide all necessary reviewer access links. *The entry may remain private before publication.*	https://www.ncbi.nlm.nih.gov/geo/query/acc.cgi?acc=GSE104686
3. Provide a list of all files available in the database submission.	YW24_vs_YW21_peaks.broadPeak YW25_vs_YW21_peaks.broadPeak YW30_vs_YW27_peaks.broadPeak YW31_vs_YW27_peaks.broadPeak YW36_vs_YW33_peaks.broadPeak YW37_vs_YW33_peaks.broadPeak YW42_vs_YW39_peaks.broadPeak YW43_vs_YW39_peaks.broadPeak
4. If available, provide a link to an anonymized genome browser session (e.g. UCSC).	Not available

Methodological details

5. Describe the experimental replicates.	ChIP-seq were performed on 2 E14.5 Mettl14 KO NSC lines and 2 E14.5 nondeleted NSC lines.
6. Describe the sequencing depth for each experiment.	On average 20 million 76-bp single-end reads per library were mapped and 70% of the reads were uniquely mapped to the reference genome.
7. Describe the antibodies used for the ChIP-seq experiments.	The antibodies used were as follows: rabbit anti-H3K27ac (Active Motif, Cat. # Ab4729, Lot. # GR312658-1) and rabbit anti-H3K27me3 (Millipore, Cat. # 07-449, Lot. # 2686928). Both antibodies are ChIP grade and used in ENCODE project (https://genome.ucsc.edu/ENCODE/antibodies.html).
8. Describe the peak calling parameters.	To align ChIP-seq DNA reads to the reference mm10 genome, we used Bowtie2 (v2.3.1) (Langmead and Salzberg 2012) with the default options except that "--broad" was turned on for calling broad peaks. Each ChIP library in each biological replicate was compared against the DNA input background library in the corresponding cell type + condition. Specifically, histone marks H3K4me1, H3K4me3, H3K27ac, and H3K27me3 in wild-type and M14 knockout (KO) mutant of mouse neural progenitor cell (NPC) were compared with the DNA input in wild-type and M14 KO NPC, respectively. Default cutoff of FDR < 0.05 were used to determine ChIP-seq peaks relative to the input libraries.
9. Describe the methods used to ensure data quality.	Default MACS peak call threshold was used to obtain peaks at FDR < 0.05. On average, 52,299 peaks were retained per library and 6368 peaks with fold-enrichments greater than 5 over the 20 ChIP-seq libraries.
10. Describe the software used to collect and analyze	R environment and custom scripts were used to collect peaks and analyze

the ChIP-seq data.	the data. Detailed methods are described in the manuscript. Scripts are available upon request.

nature research

Corresponding author(s): Jing Crystal Zhao

☐ Initial submission ☐ Revised version ☒ Final submission

Flow Cytometry Reporting Summary

Form fields will expand as needed. Please do not leave fields blank.

Data presentation

For all flow cytometry data, confirm that:

☒ 1. The axis labels state the marker and fluorochrome used (e.g. CD4-FITC).

☒ 2. The axis scales are clearly visible. Include numbers along axes only for bottom left plot of group (a 'group' is an analysis of identical markers).

☐ 3. All plots are contour plots with outliers or pseudocolor plots.

☒ 4. A numerical value for number of cells or percentage (with statistics) is provided.

Methodological details

5. Describe the sample preparation.	Mouse brain cortex were dissected out from E14.5 or E17.5 embryonic brains and triturated by pipeting. Dissociated cells were cultured as neurospheres with NeuroCult Proliferation Medium (Stemcell Tech.) before flow cytometry. Dissociated NSCs were incubated with Dead Cell Apoptosis Kit with Annexin V Alexa Fluor-488 & Propidium Iodide (Thermo Fisher Scientific) following manufacturer's protocols. Briefly cells were diluted in 1× annexin-binding buffer to ~ 1×10^6 cells/mL, add 5ul Alexa Fluor® 488 annexin V and 1 µL 100 µg/mL PI working solution to each 100 µL of cell suspension and incubate at room temperature for 15 minutes. After incubation add 400 µL 1× annexin-binding buffer and analyze the stained cells by flow cytometry.
6. Identify the instrument used for data collection.	LSRFortessa Cell Analyzer (BD Biosciences)
7. Describe the software used to collect and analyze the flow cytometry data.	FACSDiva 6 (BD Biosciences)
8. Describe the abundance of the relevant cell populations within post-sort fractions.	No sorting was involved in this study.
9. Describe the gating strategy used.	Cell debris were excluded by FSC-A/SSC-A plot and singlets were gated by SSC-A/SSC-W plot. The gates for Propidium Iodide (PI) and AnnexinV-FITC were determined by non staining cells, PI single staining cells and AnnexinV-FITC single staining cells.

Tick this box to confirm that a figure exemplifying the gating strategy is provided in the Supplementary Information. ☐